

Abstract

Nodal Modulator Is Required to Sustain Endoplasmic Reticulum Morphology

Catherine Amaya

2021

Nodal modulator (NOMO) is a widely conserved type I transmembrane protein of unknown function, with three nearly identical orthologs specified in the human genome. We identified NOMO1 in a proteomics approach aimed at the identification of proteins that support the structural integrity of the endoplasmic reticulum (ER). We have investigated the role of NOMO1 in relation to ER morphology. Overexpression of NOMO1 imposes sheet morphology on the ER. Extending NOMO1 correlatively increases the ER intermembrane distance, demonstrating the ability to regulate the ER lumen distance. Depletion of NOMO1 and its orthologs causes a collapse of ER morphology concomitant with the formation of membrane-delineated holes in the ER network. These holes are positive for the lysosome marker LAMP1. LC3-II and p62 levels are increased upon NOMO depletion, indicative of upregulation or inhibition of autophagy. *In vitro* reconstitution of NOMO1 revealed a dimeric state that is mediated by the cytosolic tail domain, with each monomer featuring a “beads on a string” shape likely representing Ig-like folds. Based on these observations and a genetic epistasis analysis including the known ER-shaping proteins Atlastin2 and Climp63, we propose a role for NOMO1 in the functional network of ER-shaping proteins.

Nodal Modulator Is Required to Sustain Endoplasmic Reticulum Morphology

A Dissertation

Presented to the Faculty of the Graduate School
of Yale University

In Candidacy for the Degree of
Doctor of Philosophy

By

Catherine Amaya

Dissertation Director: Dr. Christian Schlieker

December 2021

© 2021 by Catherine Amaya

All rights reserved.

Acknowledgements

I am grateful for the privilege and opportunity to complete this Ph.D. in the MB&B Department at Yale University. This department is full of amazing scientists willing to share their expertise and skills. I would like to thank Christian for trusting me with this ER morphology project. This project was very exploratory, but Christian allowed me to take it in any direction that would lead us closer to answers. His mentorship has allowed me to become a more confident and critical scientist.

I am also thankful for my thesis committee, Mals Mariappan and Mark Hochstrasser. Thank you for your support and guidance during my Ph.D. I have really appreciated your input and time in helping my project grow into a full story. I also want to thank Chih-Chi Andrew Hu for taking the time to read my thesis and provide feedback.

I am thankful to Morven Graham for her patience and skill in handling all the thin-section EM samples. I am also thankful to Kaifeng, Swapnil, and Chris in the Xiong lab, without which the negative stain model and SEC-MALS experiments would have not been possible.

Thank you to the members of the Schlieker lab, thank you for sharing your skills and experience in helping me with my experiments and for telling me if my images were pretty enough.

Lastly, thank you to my family for reminding me of the bigger picture in life. Thank you for your support and encouragement.

Table of Contents

Abstract	1
Acknowledgements	4
Chapter 1: An Introduction	9
1.1 Tubule shaping proteins.....	9
1.2 Disrupting tubule shaping protein functions disrupts ER functions.....	12
1.3 Importance of ER-organelle contacts	13
1.4 ER sheet shaping proteins	14
1.5 Nuclear envelope shaping proteins.....	15
1.6 NOMO1 background and Thesis overview.....	16
Chapter 2: Materials and Methods	18
2.1 Tissue Culture and Stable Cell Line Generation	18
2.2 APEX2 and Mass spectrometry	19
2.3 Immunofluorescence.....	20
2.4 Rescue Assays	21
2.5 Confocal Imaging.....	21
2.6 Bafilomycin A Assay	22
2.7 Antibodies	22
2.8 Transmission Electron Microscopy	22
2.9 Transmission Electron Microscopy Image Quantification.....	23

2.10 Cloning, Expression and Purification of NOMO proteins.....	23
2.11 Size exclusion chromatography linked to multi-angle light scattering (SEC-MALS)	24
2.12 Single Particle Electron Microscopy	25
Chapter 3: Results.....	27
3.1 Identification of NOMO1 as an abundant, ER-luminal protein.....	27
NOMO depletion results in altered ER morphology	32
Genetic interactions between NOMO and known ER-shaping proteins.....	34
Genetic complementation of NOMO domains	37
NOMO does not affect the GTPase rate of Atlastin2	40
Microtubules are excluded from the holes under NOMO depletion	41
Lipid levels under NOMO depletion	43
Ultrastructural and compositional characterization of hole phenotype.....	44
Three-dimension investigation of observed hole	47
3.2 NOMO depletion inhibits autophagy	49
3.3 Structural characterization of NOMO1	52
NOMO1 overexpression imposes ER sheet morphology.....	52
NOMO is a rod-shaped dimer.....	55
NOMO1 adopts a “beads on a string” morphology	57
NOMO regulates the ER intermembrane space	62

3.4 Investigating the role of NOMO in ER-phagy and the NE	64
NOMO1 is not likely to have a role in ER-phagy.....	64
The potential role of NOMO in the Nuclear Envelope.....	67
Chapter 4: Discussion	70
Chapter 5: Future Directions	76
References.....	81

List of Figures

Figure 1. Identification of NOMO1 as abundant and conserved ER-resident protein.	30
Figure 2. Domain organization of NOMO.	31
Figure 3. NOMO depletion results in profound changes of ER morphology.	33
Figure 4. Epistasis analysis of known ER shaping proteins and NOMO1.	36
Figure 5. Morphological effects of NOMO domains.	39
Figure 6. NOMO does not affect the AtI2 GTPase rate.	40
Figure 7. Tubulin is excluded from NOMO depletion holes.	42
Figure 8. Lipid levels under NOMO depletion.	44
Figure 9. EM analysis of NOMO and AtI2-depleted cells.	46
Figure 10. Three-dimensional morphology of the NOMO depletion hole.	48
Figure 11. Sheet disruption inhibits autophagy.	51
Figure 12. NOMO1 restricts the ER lumen.	54
Figure 13. Determination of the NOMO1 oligomeric state.	57
Figure 14. Single particle analysis of NOMO1.	59
Figure 15. The flexibility of NOMO prevents distinguishing the C-terminal end. ..	61
Figure 16. Extended NOMO constructs correlatively increase the intermembrane space.	63
Figure 17. NOMO likely does not have an ER-phagy role.	66
Figure 18. NOMO and the nuclear envelope.	69
Figure 19. Depletion of NOMO interaction partners do not disrupt ER morphology.	72
Figure 20. Models of the mechanism of NOMO regulating the ER intermembrane space.	74

Portions of this dissertation have been previously published in:

Catherine Amaya, Christopher JF Cameron, Swapnil C. Devarkar, Mark B. Gerstein, Yong Xiong, Christian Schlieker. Nodal Modulator is required to sustain endoplasmic reticulum morphology. bioRxiv 2021.01.28.428001; doi: <https://doi.org/10.1101/2021.01.28.428001>

Chapter I: An Introduction

As the largest, single-membrane bound organelle, the endoplasmic reticulum (ER) is responsible for critical and diverse functions, including lipid synthesis, folding and export of membrane and secretory proteins, and calcium storage (Ma and Hendershot, 2001; Matlack et al., 1998; Meldolesi and Pozzan, 1998). These responsibilities are divided into three structurally distinct regions, namely the nuclear envelope (NE), sheets, and tubules (Palade, 1956). For example, protein synthesis and folding are partitioned to the sheets, and organelle fission and calcium storage to the tubules (Friedman et al., 2011). The structural integrity of these regions is maintained and regulated by unique membrane shaping proteins.

1.1 Tubule shaping proteins

The membrane shaping proteins necessary to support the curvature of ER tubules have largely been established (Powers et al., 2017), which include Reticulons (RTNs), Atlastins (Atls), and receptor expression enhancing proteins (REEPs) (Hu et al., 2008; Hu et al., 2009; Voeltz et al., 2006). The prominent structural motif shared by these proteins is a transmembrane hairpin, which serves as a wedge that is inserted into the outer lipid layer of the ER membrane to impose high curvature on the membrane and help create a tubular shape. An amphipathic helix has also been found to be important for hetero-oligomerization between REEPs and RTNs (Wang et al., 2021).

Reticulon4a was the first tubule shaping protein to be identified. *In vitro* experiments of purified ER membranes were used to find a chemical inhibitor of network formation and then find the target of that chemical inhibitor, which was identified as Rtn4a

(Voeltz et al., 2006). Overexpression of Rtn4a exclusively localized to the tubular ER and created long unbranched tubules. Subsequent investigations demonstrated that adding purified Rtn1p or Yop1p (REEP5 homolog) from yeast to proteoliposomes indeed generated membrane tubules (Hu et al., 2008). Both these proteins were also identified to contain reticulon homology domains, a domain defined by two hydrophobic regions of at least 30 amino acids in length separated by a spacer of about 60 amino acids (Oertle et al., 2003), that is now referred to as the hairpin transmembrane (Wang et al., 2021).

The Atlastin protein family first became of interest because mutations in Atlastin-1 (Atl-1) were associated with early onset hereditary spastic paraplegia (HSP) SPG3A (Zhu et al., 2003). Atl-1 was recognized to have homology with dynamin proteins due to the GTPase domain Atl-1 has, the function of which was not yet understood, as well as hydrophobic regions that would make it an integral membrane protein. Once Rtn4a had been established as a tubule shaping protein, Atlastin-1 was hypothesized to be a tubule shaping protein due to the potential hairpin transmembrane the hydrophobic regions could form. Atl-1 was shown to interact with Rtn4a and Rtn3c, another reticulon isoform (Hu et al., 2009), beginning to establish Atl-1 as an ER tubule protein. Atlastin-2 and Atlastin-3 are the other two members of the Atlastin family which were identified due to having over 65% sequence homology to Atl-1 (Zhu et al., 2003). Because Atl-1 is only expressed in the brain, understanding the function of Alts in mammalian cells necessitates investigating Atl-2 and Atl-3 which are expressed in other mammalian tissues (Hu et al., 2009; Zhu et al., 2003). Depletion of Atl-2 and Atl-3 or mutations that abolishes the GTPase activity of Atl-1 were shown to cause similar extended unbranched tubules as Rtn4a overexpression (Hu et al., 2009), supporting the role of Alts in tubule

shaping. *In vitro* experiments then showed that the GTPase domain of Atls were responsible for the reticular network connections of the ER, the first understanding of the mysterious need for GTP in *in vitro* ER reconstitutions (Hu et al., 2009; Orso et al., 2009).

The GTPase cycle of Atl-1 was then investigated by solving the crystal structure of the cytosolic portion of Atl-1, which included the GTPase domain and the linker region that connects the GTPase domain to the membrane region (Bian et al., 2011; Byrnes and Sonderrmann, 2011). The mechanism showed that the Atl-1 GTPase domain dimerizes with the GTPase domain of another Atl-1 on an opposing tubule. Upon GTP hydrolysis, the GTP domains then undergo a conformational change to twist around each other, thereby bringing the opposing membranes together (Byrnes and Sonderrmann, 2011). This GTPase cycle is not always successful in causing the fusion of the tubules and it is hypothesized that the Atl dimer can go through multiple cycles of pulling the membranes together until the tubules fuse (Byrnes and Sonderrmann, 2011). Additionally, the Atl dimer can remain tethered together to keep the tubules in proximity (Byrnes and Sonderrmann, 2011).

Together, mutations in REEP1, Atl-1, and spastin, a microtubule-severing ATPase, are the cause of the majority of HSP cases. Therefore, once Atl-1 had been established as a tubule shaping protein, REEP1 and spastin were investigated as potential Atl-1 interaction partners and were indeed confirmed to interact with Atl-1 (Park et al., 2010). These interactions were dependent on the hydrophobic regions that form intramembrane hairpin structures (Park et al., 2010), suggesting there are various heterooligomeric populations in the tubules. These oligomers may be necessary to maintain the curvature of the tubules. Another potential function for these oligomers is when an Atl dimer is

pulling two tubules together. This tethered region may be causing a local area of higher curvature which may need support from more tubule shaping proteins to momentarily increase the curvature. How these oligomers would be regulated is not understood. Once tubule fusion has occurred, the local membrane curvature becomes negative. This negative curvature has shown to be stabilized by the lunapark protein, a protein that favors negative curvature and specifically localizes to three-way junctions dependent on interactions with AtIs (Chen et al., 2012; Shemesh et al., 2014; Zhou et al., 2019).

1.2 Disrupting tubule shaping protein functions disrupts ER functions

Although there is an inherent understanding of the importance of tubule shaping proteins due to the connection in causing HSP, amyotrophic lateral sclerosis, and other neurodegenerative disorders (Blackstone et al., 2011; Chiurciu et al., 2014; Park et al., 2010), there is literature on the disruption of specific ER functions caused by depleting or inhibiting the function of tubule shaping proteins. The establishment of a Rtn4a/b knockout cell line demonstrated a suppression of store-operated calcium entry (SOCE) (Jozsef et al., 2014). This was likely due to the mislocalization of STIM1, a core SOCE component, due to the decrease of tubules under Rtn4a/b KO (Jozsef et al., 2014). Mutations in spastin have also been shown to significantly decrease SOCE (Vajente et al., 2019). Additionally, an AtI1/2/3 KO cell line was established in NIH-3T3 cells to measure disturbances to cell function (Zhao et al., 2016). This cell line was sensitive to ER stressors tunicamycin and thapsigargin, amounting an ER stress response faster than the control cell line (Zhao et al., 2016). Atlastin depletion also results in smaller lipid droplets (Klemm et al., 2013). Knocking atlastin or reticulon in drosophila embryos is

lethal (Espadas et al., 2019). Lastly, depletion of REEP5 in mouse cardiac myocytes causes an upregulation of Rtn4, an apparent compensatory mechanism to prevent loss of tubule function (Lee et al., 2020).

ER-phagy is a recent field in which tubule shaping proteins also have important functions in. Rtn3L has been shown to be a crucial component of the turnover of tubular ER through a specific autophagy pathway, without which this tubule turnover pathway cannot occur (Grumati et al., 2017). AtI-2 and AtI-3 have also been shown to be part of specific ER-phagy pathways (Chen et al., 2019; Liang et al., 2018). Although disruption of these pathways does not result in global ER stress or clear disruption of ER function, once the cargo that is recycled from these pathways is identified, the importance will become clearer.

1.3 Importance of ER-organelle contacts

The ER is constantly in contact with various cellular organelles and most of these contact sites occur between the organelle and ER tubules. ER tubule contact sites with endosomes mediates the fission of endosomes (Rowland et al., 2014), which was shown to be due to the function of the TMCC1 protein family (Hoyer et al., 2018). Disrupting these contacts interrupts the trafficking of endosomes (Hoyer et al., 2018). ER-mitochondria contact sites have been shown to regulate not only mitochondrial fission, but also fusion (Abrisch et al., 2020). Dynamic-related protein 1 (Drp1) and mitochondrial fission factor (Mff) are enriched at ER-Mitochondria contact site. Depletion of either Drp1 or Mff results in elongated mitochondria but ER-mitochondria contacts still occur, therefore the mechanism of fusion or fission have not been determined but the observable

tubule wrapping around and constricting the mitochondria is undeniable (Friedman et al., 2011). ER contact sites also serve as P Body maturation sites and fission sites for ribonucleoprotein (RNP) granule fission (Lee and Bahmanyar, 2020). The mechanism is not yet understood but it was an exciting observation as P Bodies and RNP granules do not have membranes. Disrupting ER morphology indirectly disrupts these necessary ER-organelle contact sites.

1.4 ER sheet shaping proteins

Although tubule shaping proteins have been well established, our understanding of sheet morphology is less developed. Sheets are defined by large flat membrane areas with high curvature edges (Shemesh et al., 2014). The high curvature edges of the sheets are enriched of Rtns (Jozsef et al., 2014; Schroeder et al., 2019; Voeltz et al., 2006). Depleting Rtn4 allowed a striking proliferation of sheets (Jozsef et al., 2014) demonstrating how the ratio of sheets versus tubules is dependent on the presence of tubule proteins.

The maintenance of sheet spacing is largely attributed to cytoskeleton linking integral membrane protein 63 (Climp63), an ER-microtubule binding protein that features a long coiled-coil domain in the ER lumen (Klopfenstein et al., 1998; Shibata et al., 2010; Vedrenne et al., 2005). Climp63 was proposed to be a sheet shaping protein because of the high abundance of Climp63 in secretory cells and in differentiated B cells (Shibata et al., 2010). The extended coiled-coil domain of Climp63 was hypothesized to dimerize across the ER lumen to support an intermembrane space of ~60 nm (Shibata et al., 2010). Indeed, modulating the length of the Climp63 coiled-coil domain has been shown to

correlatively change the ER luminal distance (Shen et al., 2019). Kinectin and p180 have also been proposed to contribute to the flatness of sheets due to their high abundance in differentiated B cells, but simultaneous depletion of Kinectin, p180, and Climp63 or Climp63 alone does not result in a loss of sheets (Shibata et al., 2010). Rather, the ER diameter is uniformly decreased to 30 nm upon Climp63 depletion (Shen et al., 2019; Shibata et al., 2010). Climp63 has also been computationally modeled to function in keeping the opposing sheet membranes from collapsing into each other (Schweitzer et al., 2015). However, Climp63 depletion does not lead to a loss of sheets, and no functional perturbations of the ER have been reported. These observations suggest that additional, yet unidentified, sheet shaping proteins may exist to support ER sheet functions.

1.5 Nuclear envelope shaping proteins

The nuclear envelope (NE) is part of the ER membrane network as the outer nuclear membrane (ONM) is continuous with the ER membrane. The spacing of the nuclear envelope was predicted to be regulated by the linker of nucleoskeleton and cytoskeleton (LINC) complex, which is composed of Sad1 and Unc-84 (SUN) proteins integral to the inner nuclear membrane (INM) and Klarsicht, ANC-1 and Syne homology (KASH) proteins localized in the ONM. Depletion of Unc-84 in *C. elegans* demonstrated that the nuclear envelope spacing was not affected except in muscle cells, where the nuclear envelope was found to have a significantly increased intermembrane spacing (Cain et al., 2014). Shortening Unc-84 by 300 amino acids also had no effect on the observable spacing of the nuclear envelope (Cain et al., 2014). Therefore, it remains

unknown which proteins might be responsible for the intermembrane spacing of the nuclear envelope.

1.6 NOMO1 background and Thesis overview

In this thesis, I have identified Nodal modulator 1 (NOMO1), a widely conserved type1 transmembrane glycoprotein, as having an important function in maintaining ER sheet morphology. NOMO was first identified in zebrafish as a nodal signaling regulator (Haffner et al., 2004). The nodal signaling pathway is an embryonic developmental signaling pathway important for cellular differentiation (Shen, 2007). In this initial identification, ectopic expression of NOMO and Nicalin (NCLN), a NOMO binding partner, led to cycloptic embryos in zebrafish (Haffner et al., 2004). Transmembrane protein 147 (TMEM147) was later found to form a complex with NOMO and NCLN (Dettmer et al., 2010). The first potential functions of NCLN and TMEM147 were recently identified when NCLN and TMEM147 were shown to be in a complex with Sec61. This complex was linked to a role in membrane protein biogenesis (McGilvray et al., 2020). However, the solved structure of this complex did not contain NOMO1, leaving the molecular function of NOMO unresolved. Subsequent literature on NOMO have linked NOMO to roles in cell proliferation in human trophoblast cells and colorectal cancer (Gao et al., 2012; Perea et al., 2017) and cell differentiation of cardiomyocytes (Zhang et al., 2015), but the molecular basis of the observed NOMO phenotypes remained undiscovered.

Herein, I explored various avenues for the effect of NOMO overexpression and depletion on ER morphology. I have demonstrated that depletion of NOMO1 causes a drastic perturbation of ER morphology, while the overexpression of NOMO imposes a

defined intermembrane spacing on the ER. Genetic epistasis analysis with AtI2 and Climp63 support NOMO having a role in shaping the ER. Genetic epistasis analysis with various domains of NOMO revealed additional ER morphology phenotypes that could help further understand the role of NOMO in the context of potential microtubule and lysosome interactions. Additionally, *in vitro* reconstitution including light scattering and low-resolution electron microscopy (EM) collectively suggest that NOMO1 is a dimer of rod-shaped molecules, featuring Ig-folds that are arranged as “beads on a string”. Based on these observations, I propose a role of NOMO1 in functional network of proteins responsible for establishing and maintaining the morphology of the ER.

Chapter 2: Materials and Methods

2.1 Tissue Culture and Stable Cell Line Generation

U2OS and HeLa cells from ATCC were maintained at 37°C, 5% (vol/vol) CO₂ and regularly passaged in DMEM media supplemented with 10% (vol/vol) Fetal Bovine Serum (Gibco) and 1% (vol/vol) Penicillin/Streptomycin (Gibco). Expi293F cells were maintained at 37°C, 8% CO₂ in Expi293F Expression Media and passaged to maintain a density of less than 8 million cells per mL.

U2OS and HeLa cells were transfected with plasmids using X-tremeGene9 or Fugene-6, according to the manufacturer's protocol, 24 hours before fixing with 4% paraformaldehyde in phosphate buffered solution (PBS).

For siRNA transfections, RNAi Lipofectamine was used to transfect U2OS and HeLa cells. siRNA was used at a final sample concentration of 50 nM. A double dose protocol was followed for NOMO and Climp63 depletion where the cells were transfected with siRNA on the first day, transfected again with siRNA 24 hours later, and fixed with 4% (vol/vol) paraformaldehyde in PBS 48 hours after the second transfection.

NOMO and Climp63 were depleted with ON-TARGETplus SmartPools from Dharmacon. Atlastin2 was depleted using the siRNA as in (Pawar et al., 2017).

Retroviral stable cell lines were generated with the Retro-X Tet-On advanced inducible expression system (Takara Bio). To produce retrovirus, low-passage 293T cells were transfected with the following DNA plasmids: 2 µg MMLV gag/pol, 1 µg viral envelope protein VSV-G, and either 6 µg of pRetroX-Tight-Pur-mScarlet-sec61β or pRetroX-Tet-On using X-tremeGENE 9 (Roche). Supernatants were harvested 72 hrs later, filtered

with a 0.45 µm filter unit, and stored at -80°C. U2OS cells were seeded in a six-well plate 24 h before transduction. Cells were transduced with both viruses in the cCulture medium was supplemented with 4 µg/mL polybrene (Sigma-Aldrich). After 48 hrs, cells were trypsinized and transferred to a 10-cm plate with medium supplemented with 1 µg/mL puromycin and 800 µg/mL Geneticin (Thermo Fisher Scientific). Cells were left under antibiotic selection for 10 days before plating single colonies and selecting by expression via immunofluorescence imaging.

2.2 APEX2 and Mass spectrometry

ER-APEX2 was transfected into 2 x 10 cm plates of HeLa cells using XtremeGene-9 and expressed overnight. 16-18 hr later, cells were incubated with 500 µM biotin-phenol for 30 min and then treated with 1 mM hydrogen peroxide, from a freshly diluted 100 mM stock, for 1 min before being quenched with 2x quenching buffer. 2x quenching buffer contained 50 mg Trolox and 80 mg sodium ascorbate in 20 mL of phosphate buffered solution (PBS). Cells were rinsed with 1x quenching buffer twice and once with PBS. One control plate was not treated with hydrogen peroxide, but was still rinsed with 1x quenching buffer and PBS. 0.05% Trypsin was then added to the cells for collection into a microfuge tube. Cell samples were spun down at 800 g, 3 min, 4°C, rinsed once with PBS, spun down again at 0.8 g, 3 min, 4°C, then lysed in an SDS buffer, before quantifying protein concentrated with a BCA Assay (Thermo Fisher). The original protocol can be found in (Hung et al., 2016). Equal amount of lysate samples were incubated with 30 µL streptavidin resin for 3 hours. The beads were washed 3 times and then eluted using 2 x Laemmli Sample Buffer (Bio-Rad). The elution was subjected to SDS PAGE to run the

sample into the lane. The lane was then excised into two to three bands and submitted for mass spectrometry analysis.

Mass spectrometry samples were analyzed by the Mass Spectrometry (MS) & Proteomics Resource of the W.M. Keck Foundation Biotechnology Resource Laboratory located at the Yale School of Medicine. An LTQ-Orbitrap XL was used (Thermo Scientific). The HeLa cell ER-APEX2 Mass Spectrometry Dataset has been made available at <https://zenodo.org/record/4721623#.YlcSEuhKhyw>.

2.3 Immunofluorescence

Imaged cells were fixed in 4% (vol/vol) paraformaldehyde/PBS for 15 minutes and permeabilized with 0.1% Triton X-100/PBS for 10 minutes before blocking with 4% (wt/vol) BSA/PBS for another 10 minutes. Samples were then incubated with primary antibodies diluted to 1:500 in 4% BSA/PBS and secondary antibodies diluted to 1:700 in 4% BSA/PBS for one hour each. Samples were rinsed three times with PBS between and after antibody incubations and mounted onto slides using Fluoromount-G (Southern Biotech).

For samples where the LAMP1 antibody was used, a gentle permeabilization method was followed. After being fixed in 4% (vol/vol) paraformaldehyde/PBS for 10 min, cells were gently permeabilized with a solution of 0.05% (wt/vol) saponin and 0.05% (vol/vol) NP-40/ PBS for 3 min. The cells were then rinsed with 0.05% saponin/PBS and incubated with primary and secondary antibodies respectively diluted in 0.05% saponin, 1% BSA/ PBS. Samples were then rinsed with PBS, mounted onto slides using Fluoromount-G, and allowed to dry for at least four hours before imaging.

2.4 Rescue Assays

The rescue assays shown in Fig. 2 and 4 were done as follows. 60,000 U2OS cells were plated on a coverslip in a 12-well dish. The next day, samples were transfected. For each sample, 50 nM of the respective siRNA was incubated with 500 ng of the respective DNA in 50 uL of opti-MEM for 5 min. At the same time, 2 uL of Lipofectamine 2000 (Invitrogen) was diluted into 50 uL of opti-MEM. After 5 min, the diluted Lipofectamine was added to the siRNA/DNA and gently mixed. The mixture was left to incubate for 20 min at room temperature. Each 12-well was replaced with 900 uL of fresh media. The siRNA/DNA/Lipofectamine mixture was gently added to the well. The media was replaced 12-16 hours later. The cells were fixed 48 hours after the initial transfection. The samples were then processed for immunofluorescence and imaged on our episcopes. A minimum of 100 transfected cells were imaged for each sample for each replicate. Cells with two or more holes of 3 um or greater were considered to have the hole depletion phenotype and considered not rescued. The four relevant plasmids, NOMO1r-FLAG, Climp63-FLAG, Alt2-FLAG, AtI2K107A-FLAG, were blinded by a fellow lab member before transfections occurred. This experiment was repeated four times for each siRNA and plasmid combination.

2.5 Confocal Imaging

Immunofluorescent images were acquired on a Zeiss LSM 880 with Airyscan capabilities using a 63x objective. The pinhole size used is [I forgot to check]. A gain of less than 700 was used for each channel in each image used. ImageJ was used to crop the images if necessary. The scale bar was also inserted using ImageJ as the embedded metadata allowed for ImageJ to add the appropriately sized scale bar.

2.6 Bafilomycin A Assay

U2OS cell samples were treated with 25 μ M Bafilomycin A (Sigma), a vacuolar H^+ -ATPase inhibitor, for 4 hours. This treatment was chosen by starting with concentrations cited in the literature for U2OS cells (Coutts and La Thangue, 2015; Duan et al., 2015). Then, a range of concentrations was tested for a 4 to 5 hours duration. Cell samples that had no apparent cell death were subjected to SDS-Page/ Western Blotting to determine which concentration resulted in an LC3-II increase compared to control. The lower Bafilomycin A concentrations used for HeLa cells, 25 nM, did not cause an increase in LC3-II when used on U2OS cells. The Bafilomycin A stock was made at 1 mM in DMSO. Cell samples were then trypsinized, spun down for 3 min and 800 g, and lysed in a 1% SDS buffer. 0.25 μ L of benzonase was added to each sample. The sample was left to incubate at room temperature for 10 min before heating at 60°C for 5 min before performing a BCA assay to determine protein concentration. 10 mg per sample were loaded onto an Any KD gel for optimal resolution.

2.7 Antibodies

The antibodies used include the following: Protein disulfide isomerase (PDI), Abcam, ab2792. BiP, Abcam, ab21685. Actin, Abcam, ab8226. Alpha-Tubulin, Sigma, T5168. LAMP1, BioLegend, 328602. Calnexin, Abcam, ab75802. FLAG, Sigma, F1804. LC3, Novus, NB100-2331.

2.8 Transmission Electron Microscopy

The Center for Cellular and Molecular Imaging Electron Microscopy Facility at Yale School of Medicine prepared the samples. Cells were fixed in 2.5% (vol/vol) glutaraldehyde in 0.1 M sodium cacodylate buffer plus 2% (wt/vol) sucrose, pH 7.4, for

30 min at room temperature and 30 min at 4°C. After rinsing, cells were scraped in 1% (wt/vol) gelatin and centrifuged in a 2% (wt/vol) agar solution. Chilled cell blocks were processed with osmium and thiocarbohydrazide-osmium liganding as previously described (West et al, 2010). Samples were incubated overnight at 60°C for polymerization. The blocks were then cut into 60-nm sections using a Leica UltraCut UC7 and stained with 2% (wt/vol) uranyl acetate and lead citrate on Formavar/carbon-coated grids. Samples were imaged using a FEI Tecnai Biotwin at 80 kV, equipped with a Morada CCD and iTEM (Olympus) software for image acquisition.

2.9 Transmission Electron Microscopy Image Quantification

The intermembrane spaces quantified in the manuscript were quantified from EM images. A minimum of 15 cells were quantified for each sample. As a cell was imaged, the image acquisition software embedded the appropriate scale bar. The images were opened on a 20-inch monitor and analyzed with ImageJ. The embedded scale bar was used to set the scale bar in ImageJ. The line tool was then used to manually measure the intermembrane distance of the visible ER cross sections. A measurement was taken for every inch of visible ER cross-section. If a total of more than 150 measurements were measured from a total of 15 cells or more, the measurements were assigned a random number using the Excel random number function and the first 150 measurements were used for quantification.

2.10 Cloning, Expression and Purification of NOMO proteins

The following constructs were cloned using Gibson assembly from Dharmacon plasmids containing the original gene into a pcDNA3.1+ vector with a C-terminal FLAG tag: NOMO1-FLAG, FLAG-CLIMP63, AtI2-FLAG. NOMO^{LD}-FLAG was subcloned from

NOMO1-FLAG using Gibson assembly to include only residues 1-1160. FLAG-NOMO1 was cloned using the Dharmacon cDNA to PCR residues 33-1226 into a pcDNA3.1+ vector with an N-terminal MHC I signal sequence followed by a FLAG tag. 2xlumen-NOMO was cloned using Gibson assembly to insert another copy of the luminal domain, residues 22-1160, with a GSGS linker between the two luminal domains. 2xCD4-NOMO1-FLAG was cloned by synthesizing the 2xCD4 insert with IDT. The 2xCD4 insert is two copies of residues 1-363 of CD4 with a GSGS linker between the two copies, as well as a GSGS linker before and after the 2xCD4 insert. Gibson assembly was then used to insert the 2xCD4 fragment in between the NOMO luminal domain and transmembrane domain.

Expi293F cells were transfected with the construct of interest using the ExpiFectamine 293 Transfection Kit (Gibco) following the manufacturer's protocol for a 50 mL culture. Cells were harvested 72 hours post transfection and frozen at -80°C. Cell pellets were thawed on ice and lysed in Buffer A (50 mM MES, 100 mM NaCl, 50 mM KCl, 5 mM CaCl₂, pH 6.0), 5% glycerol, and 1% DDM for 1 hour at 4°C. Afterwards, samples were spun for 30 minutes at 20,000 g, 4°C. The supernatant was incubated with anti-FLAG M2 beads (Sigma) overnight and then loaded into a gravity column for washing before incubating with elution buffer containing 5 µM FLAG peptide for 30 min. The elution was then concentrated to 0.5 mL and subjected to size exclusion chromatography in an S200 or S75 column (GE healthcare). 0.05% DDM was added to Buffer A for full length NOMO and 0.005% DDM for NOMO^{LD}, 2XFLAG-MBP-CYT, and 2XFLAG-MBP.

2.11 Size exclusion chromatography linked to multi-angle light scattering (SEC-MALS)

Multiangle laser light-scattering experiments were performed at room temperature in a 50 mM MES pH (6.0), 150 mM KCl, 5 mM MgCl₂, 5 mM CaCl₂, 2% (vol/vol) glycerol, 0.05% (wt/vol) DDM buffer. Light-scattering data were collected using a Dawn Heleos-II spectrometer (Wyatt Technology) coupled to an Opti-lab T-rEX (Wyatt Technologies) interferometric refractometer. Samples (500 μ L) were injected and run over a Superose 6 Increase 10/300 GL column (GE Healthcare) at a flow rate of 0.5 ml/min. Light scattering (690 nm laser), UV absorbance (280 nm), and refractive index were recorded simultaneously during the SEC run. Before sample runs, the system was calibrated and normalized using the isotropic protein standard, monomeric bovine serum albumin. Data were processed in ASTRA software as previously described (Wyatt, 1993).

2.12 Single Particle Electron Microscopy

3.5 μ L of purified NOMO1-FLAG or NOMO Δ TM-FLAG were negatively stained using 2% uranyl acetate solution on carbon film, 400 mesh copper grids that were glow discharged. Grids were imaged on a FEI Talos L120C Electron Microscope (Thermo Fisher Scientific) at 120 kV. Micrographs were captured at a magnification of 73,000x. 82 and 61 micrographs were taken for NOMO and NOMO deltaTM, respectively. TIFF files were cropped to 4096x4096 pixels and converted to MRC format using the EMAN2 v2.3 (Tang et al., 2007) *eproc2d* program. 2D classifications and 3D reconstructions were produced using RELION v3.08 (Scheres, 2012) with manually picked particles. CTF estimation was performed using CTFFIND-4.1 with box sizes of 512 and 352 pixels for NOMO and NOMO deltaTM, respectively. Particles were extracted, then downsampled four-fold for 2D class averages. Selected 2D classes used for 3D reconstruction are shown in Fig. 8. Final 3D

volumes were generated by applying masks generated from initial models and auto-refinement in RELION.

Chapter 3: Results

3.1 Identification of NOMO1 as an abundant, ER-luminal protein

To identify potential sheet shaping proteins, we employed a proximity ligation approach. Previous proteomes of the ER were obtained by subcellular fractionation-based techniques that encompassed the entire ER membrane network (Chen et al., 2010a; Sakai et al., 2009), whereas we were specifically interested in the ER lumen. To this end, we used an engineered monomeric peroxidase (APEX2) (Lam et al., 2015). In the presence of hydrogen peroxide, APEX2 creates biotin-phenoxy radicals that will biotinylate proteins in a 20 nm radius (Hung et al., 2016; Hung et al., 2014; Rhee et al., 2013). We employed ER-APEX2, a construct previously shown to specifically localize to the ER lumen by virtue of a signal sequence (Lee et al., 2016). This construct was expressed in HeLa cells that were then incubated with biotin and treated with hydrogen peroxide to conjugate biotin to ER luminal proteins. The control sample was transfected with ER-APEX2 but no hydrogen peroxide was added. The treated cells were lysed in SDS buffer, and a streptavidin bead resin was used to isolate biotinylated proteins. To control for labeling efficacy, samples were eluted and subjected to SDS-PAGE and blotting using a streptavidin conjugate for detection. Since robust, hydrogen-peroxide dependent labeling was observed for a variety of proteins (Fig. 1A), we performed an analogous experiment on a larger scale and analyzed the resulting eluates via mass spectrometry following tryptic digestion. As expected, the most abundant species identified included constituents of ER protein synthesis and folding machinery (Fig. 1B), including the ER chaperones BiP, PDI, Endoplasmic reticulum chaperonin and CCD47, all of which are known residents of the ER lumen (Chitwood and Hegde, 2020; Helenius and Aebi, 2004). In

addition, NOMO2 and NOMO1 were the eighth and ninth most abundant proteins identified as judged by spectral counts, with high sequence coverage (48%) (Fig. 1 B).

NOMO1 is a type I transmembrane protein that is conserved across all metazoans (Haffner et al., 2004). Notably, NOMO homologs are also present in plants, both in monocotyledones (*Zea mays*) and dicotyledons (*Arabidopsis lyrata*) (Fig. 1C). While other metazoan organisms specify a single copy of NOMO, three copies of NOMO are present in the human genome designated: *NOMO1*, *NOMO2*, and *NOMO3* (Yates et al., 2019). *NOMO1* and *NOMO2* specify a 134 kDa membrane protein composed of an N-terminal signal sequence followed by a 1124 residue luminal domain, a transmembrane domain, and a short, 40 residue cytosolic domain. The luminal domains of the three proteins are identical except for six amino acids (Fig. 2A). *NOMO2* has a cytosolic domain that is 45 residues longer than *NOMO1* and *NOMO3*, resulting in a 139 kDa membrane protein. This extremely high similarity suggests that NOMO orthologs have arisen from recent gene duplication events and have identical or similar cellular functions.

To begin to understand which function NOMO might have in the ER, we employed BLAST searches, secondary structure predictions, and fold recognition programs to identify homology to proteins of known structure. While these searches did not reveal related human proteins, *NOMO1* was predicted to form a beta sheet-rich structure (Fig. 2B) by PSIPred (Buchan and Jones, 2019). Consistently, a significant structural degree of similarity was detected between *NOMO1* and several bacterial Ig-like fold proteins. The highest similarity was observed for BaTIE, a sortase-anchored surface protein from *Bacillus anthracis* (Miller et al., 2018), featuring 4 tandem Ig domains of 19 nm in length. Phyre2 (Kelley et al., 2015) modeled *NOMO1* residues 58-398 with 99% confidence,

predicting 4 consecutive Ig folds for this region (Fig. 1D). This structural homology to bacterial pili proteins led us to hypothesize that NOMO1 might adopt an extended rod structure that could serve as a structural component to support membrane spacing.

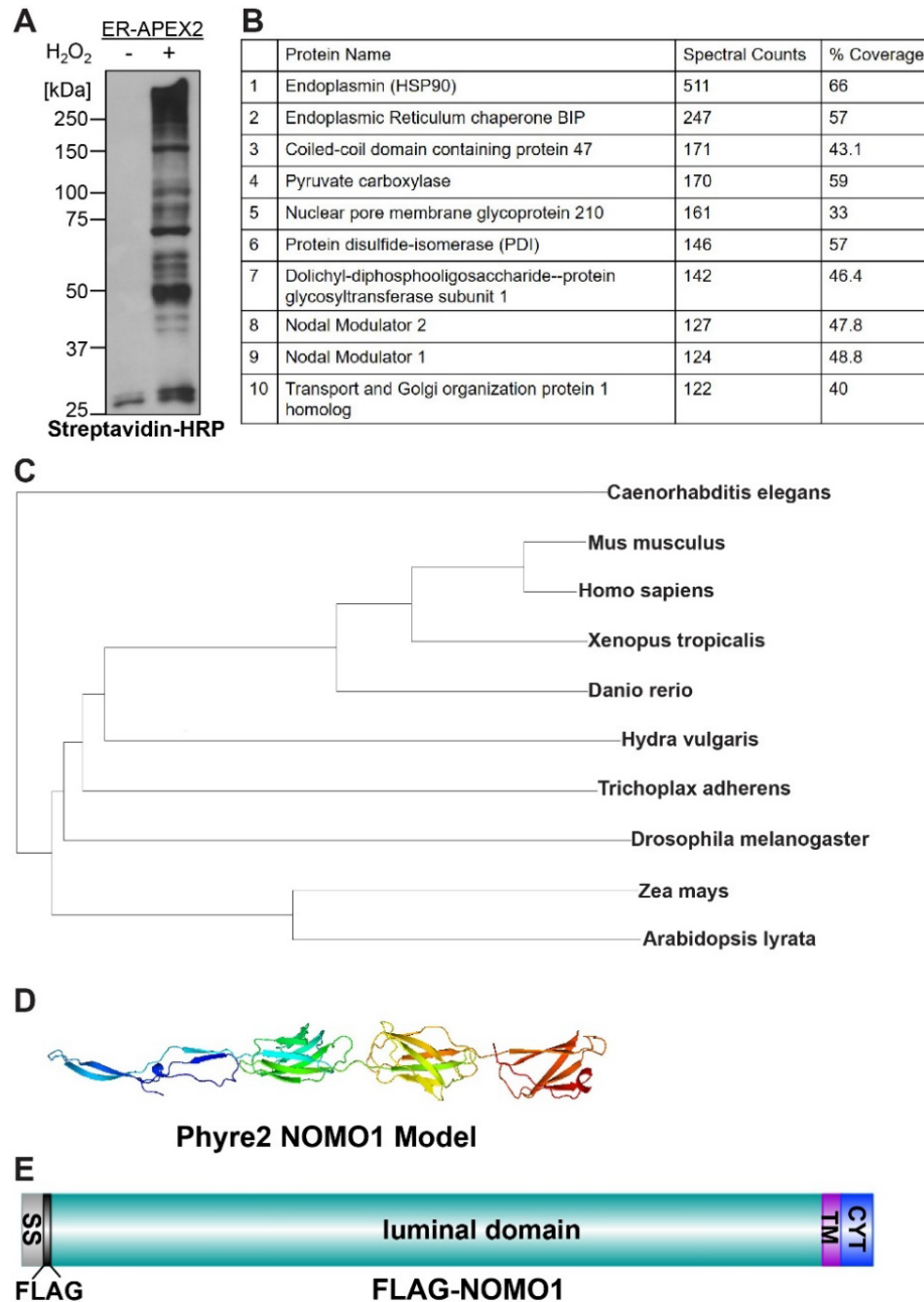


Figure 1. Identification of NOMO1 as abundant and conserved ER-resident protein.

A. Cells expressing ER-APEX2 were treated with biotin-phenol in the absence or presence of hydrogen peroxide, lysed and subjected to western blotting using streptavidin-HRP. B. Table of top ten most abundant proteins from mass spectrometry analysis in order of spectral count; % Coverage is the sequence coverage of the protein based on peptide sequences identified. C. Phylogenetic tree of NOMO1 homologs in indicated metazoan and plant species. D. Phyre2 model of NOMO1, residues 58-398. E. FLAG-NOMO1 domain structure. The FLAG tag was inserted between the cleavable signal sequence (SS) and the luminal domain. TM, transmembrane domain, CYT, cytosolic tail.

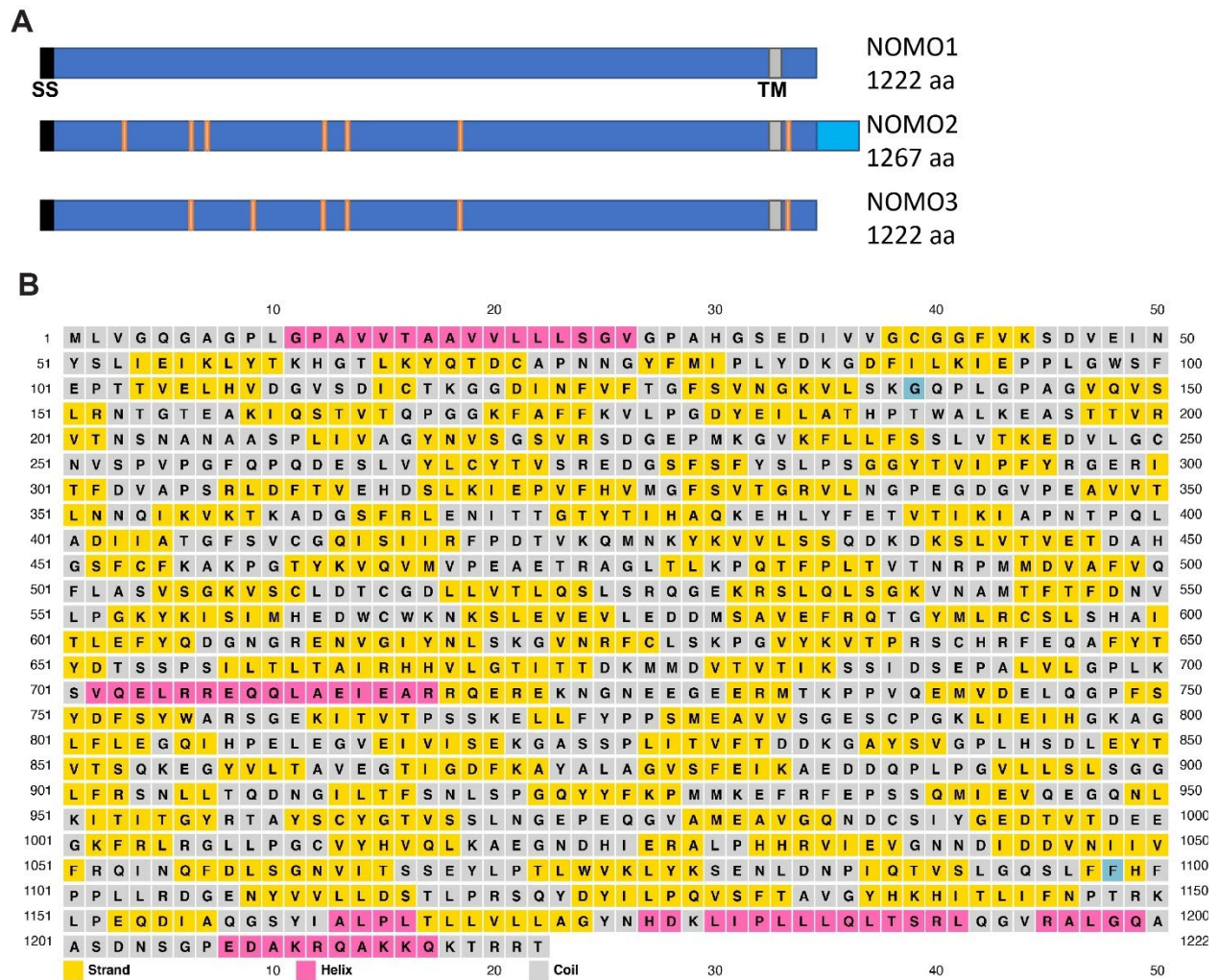


Figure 2. Domain organization of NOMO.

A. Comparison of NOMO1, NOMO2, and NOMO3 isoforms. Orange denotes single amino acid differences between isoforms. Light blue region denotes the extended tail of NOMO2. SS= signal sequence. B. NOMO1 secondary structural prediction from PSIPRED.

NOMO depletion results in altered ER morphology

As a first test to determine if NOMO depletion affects ER morphology, we depleted NOMO in U2OS and HeLa cells using siRNA. Due to the high genomic similarity between *NOMO1*, *NOMO2*, and *NOMO3*, siNOMO1 targets all three corresponding mRNAs. In the rest of this thesis, I will refer to the experimental condition simultaneously depleting NOMO1, NOMO2, and NOMO3 as siNOMO. The canonical nomenclature of NOMO1 will be used for experiments based on the specific NOMO1 cDNA or protein. NOMO depletion caused a striking rearrangement of the ER network and large holes in the ER up to 8 μm in diameter were visible by immunofluorescence microscopy (Fig. 3A). Because the phenotype was observed in both HeLa and U2OS cells, U2OS cells were chosen to continue IF experiments with due to their larger ER area. Attempts at generating a CRISPR/Cas9 NOMO KO cell line were unsuccessful. While single cell colonies were obtained in which the hole phenotype was visible (Fig. 3E), cells were not viable in culture after several passages, suggesting an important, if not essential function.

To demonstrate that the siRNA-induced phenotype was specifically due to NOMO depletion, a NOMO1 rescue construct, FLAG-NOMO1r, was designed by introducing silent mutations into the targeting site of siRNA #3 of siNOMO2. This siRNA #3 depleted NOMO mRNA by over 90% as quantified by qPCR (Fig. 3B). FLAG-NOMO1r reproducibly reduced the ER phenotype from 68% penetrance to 20%, providing further evidence that the hole phenotype observed is specifically caused by NOMO depletion (Fig. 3C, D). Since the simultaneous depletion of all three NOMO orthologs can be rescued by FLAG-NOMO1r alone, we conclude that NOMO1 has a major function in the context of ER morphology.

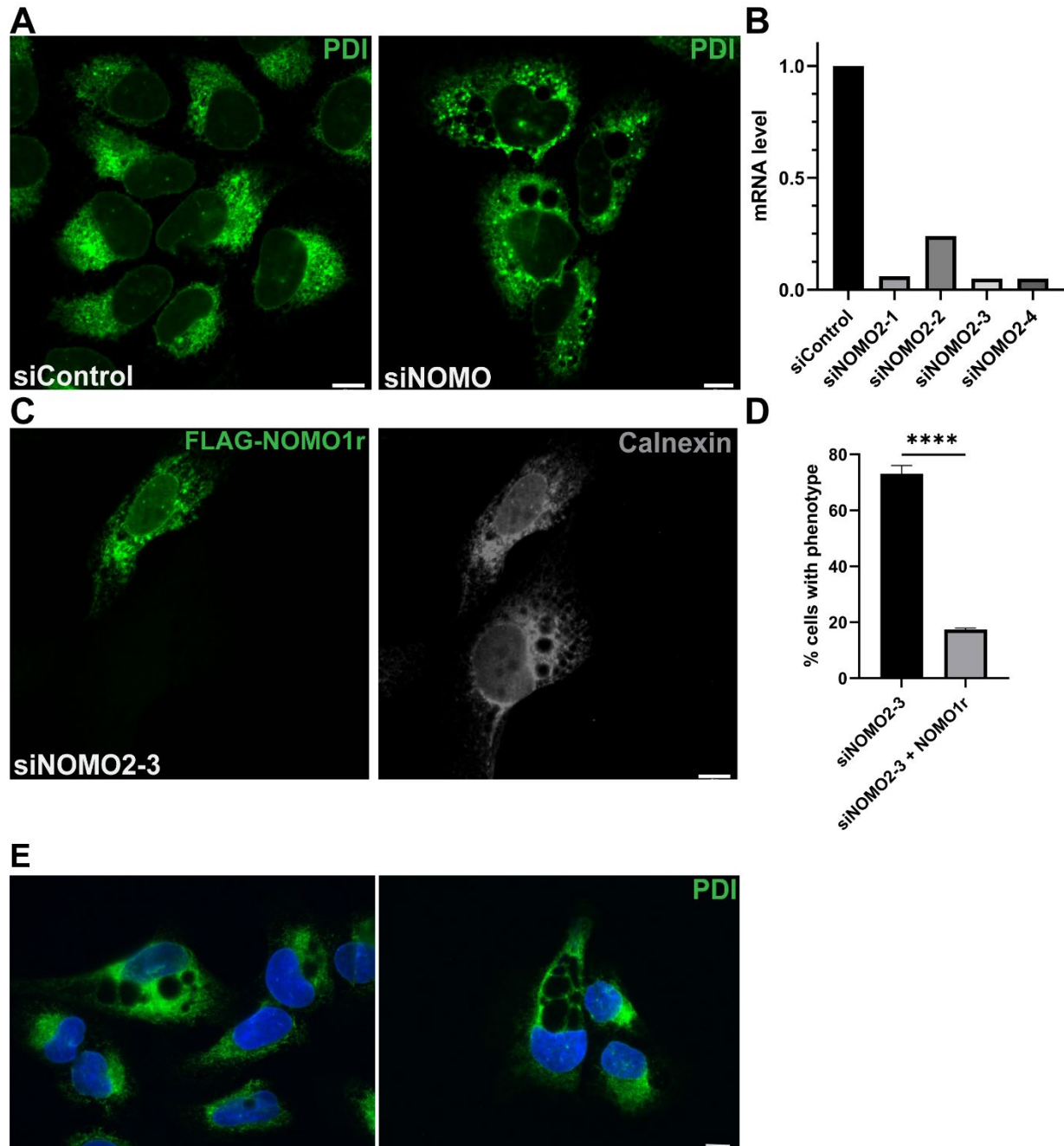


Figure 3. NOMO depletion results in profound changes of ER morphology.

A. U2OS cells were transfected with the respective siRNA for 48 hours. B. Quantification of the NOMO mRNA level after treatment with each NOMO siRNA by qPCR. C. Representative image of phenotypic rescue of the NOMO knockdown phenotype by an siRNA-resistant construct, FLAG-NOMO1r. D. Quantification of rescuing ability of FLAG-NOMO1r, $n=100$, $N=3$. Asterisks denote $P<0.005$ compared to control. Error bars indicate standard deviation. E. Representative images of two isolated NOMO KO colonies screened for the NOMO phenotype. All scale bars are 10 μm .

Genetic interactions between NOMO and known ER-shaping proteins

From a topological perspective, the predicted domain architecture of NOMO is reminiscent of the structural domain composition of Climp63 that includes a sizeable luminal domain expanding into the ER lumen, a transmembrane domain, and a short cytosolic tail (Vedrenne et al., 2005). Therefore, we sought to compare whether Climp63 depletion caused similar defects in ER morphology as NOMO depletion. Depletion of AtI2 was included as a tubule shaping protein for comparison. Surprisingly, AtI2 depletion resulted in strikingly similar holes as those caused by NOMO depletion, while Climp63 depletion had no effect on ER morphology when visualized by immunofluorescence microscopy (Fig. 4A).

Next, we asked if NOMO exhibits genetic interactions with AtI2 or Climp63. First, we tested whether the overexpression of these known ER-shaping proteins modulates the observed hole phenotype. We transfected AtI2-FLAG into NOMO depleted cells and observed that AtI2-FLAG overexpression could significantly rescue the NOMO knockdown phenotype (Fig. 4B, C). Since AtI2 is required for ER fusion, we hypothesized that the fusogenic activity is required for this effect. To this end, a rescue assay was performed with a GTPase mutant of AtI2 that cannot fuse ER membranes, AtI2 K107A (Morin-Leisk et al., 2011). This AtI2 mutant did not rescue the NOMO knockdown hole phenotype (Fig. 4C), indicating that the rescue ability of AtI2 relies on the fusogenic activity. Furthermore, in an analogous experiment, we found that Climp63-FLAG also reduced the presence of the NOMO depletion phenotype, but less than AtI2-FLAG did (Fig. 4C). These results suggest that because the NOMO depletion phenotype can be

rescued by overexpressing known ER shaping proteins, NOMO has a function in supporting ER structure.

Lastly, since *Atl2* depletion results in a similar hole phenotype, we performed the reciprocal rescue assays of co-transfecting NOMO1-FLAG or Climp63-FLAG into *Atl2* depleted cells. We found that NOMO-FLAG and Climp63-FLAG both significantly reduced the penetrance of the *Atl2* depletion phenotype (Fig. 4D, E). In conclusion, the observed genetic interactions among NOMO1, Climp63, and *Atl2* are consistent with the interpretation that NOMO contributes to the elaborate network of ER-shaping proteins.

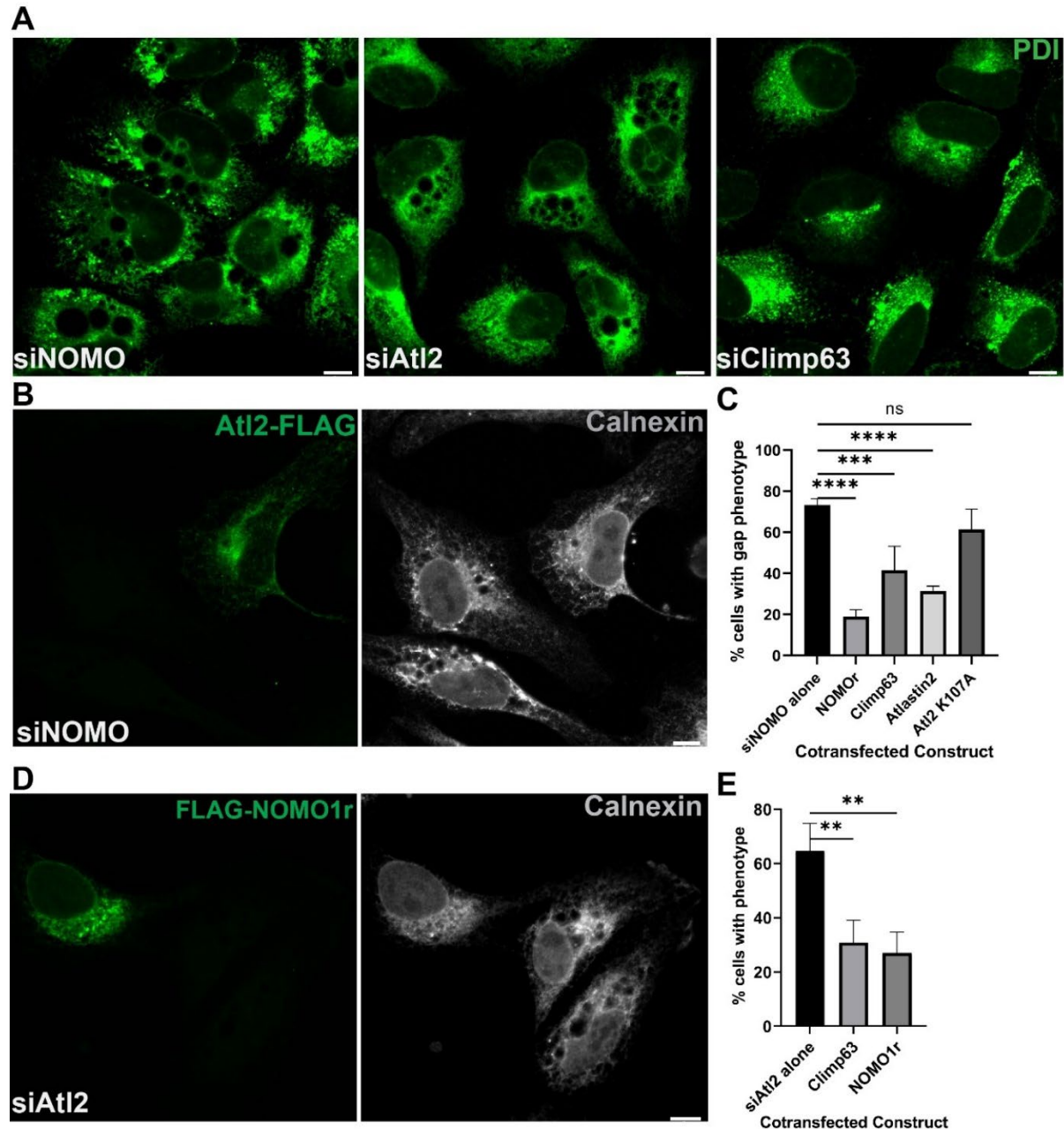


Figure 4. Epistasis analysis of known ER shaping proteins and NOMO1.

A. U2OS cells were treated with respective siRNA for 48 hours; protein disulfide isomerase (PDI) was used as the ER marker. B. Representative image of AtI2-FLAG overexpression (left panel) rescuing the NOMO KD phenotype as judged by PDI staining (right panel). C. Quantification of the ability of ER shaping proteins to rescue the NOMO KD ER phenotype, $n=100$, $N=3$. Error bars indicate standard deviation. D. Representative image of FLAG-NOMO1r overexpression (left panel) rescuing AtI2 KD phenotype (right panel). E. Quantification of NOMO1 and Climp63 overexpression rescuing the AtI2 KD phenotype, $n=100$, $N=3$. Error bars indicate standard deviation. Asterisks denote $P<0.005$. Scale bars are 10 μm .

Genetic complementation of NOMO domains

To determine which domains of NOMO1 could be important to the ability to rescue the NOMO depletion phenotype, the following constructs were designed: NOMO^{LD}, consisting of only the luminal domain, NOMO Δ CYT, lacking the cytosolic tail, and NOMO-TMCYT, lacking the luminal domain (Fig. 5A). NOMO Δ CYT had extremely low expression and the rescue ability could not be quantified. Although the rescue abilities were able to be quantified for the remaining two constructs in terms of whether there were multiple holes present in the ER or not (Fig. 5B), NOMO^{LD} and NOMO-TMCYT caused other rearrangements of the ER network. NOMO^{LD} caused the ER network to present as small circles (Fig. 5C). These small circles were reminiscent of lysosomes, so I used a lysosome associated protein 1 (LAMP1) antibody to determine if NOMO^{LD} was colocalizing with lysosomes. Indeed, NOMO^{LD} colocalized with lysosomes (Fig. 5C). NOMO^{LD} does not contain any canonical lysosome localization signals so the construct may likely be interacting with a lysosomal protein.

Under FLAG-NOMO-TMCYT overexpression, the ER network appeared to have elongated tubules which was reminiscent of microtubule localization (Fig 5D). I used a tubulin antibody to determine if FLAG-NOMO-TMCYT colocalized with microtubules and significant colocalization was observed (Fig. 5D). This suggested that the cytosolic domain may be binding to microtubules. To test if the cytosolic domain could directly bind to microtubules, a construct was designed, 2xFLAG-GFP-CYT, to use for a microtubule pelleting assay. This protein was expressed and purified from Expi293F cells. Unfortunately, this protein pelleted without any microtubules present, causing the assay to be inconclusive (Fig. 5E). To overcome this limitation, a microtubule binding assay was

done using Total Internal Reflection Fluorescence (TIRF) Microscopy. Microtubules were flowed through a small chamber and allowed to settle. The 2xFLAG-GFP-CYT protein was then gently flowed over the microtubules and allowed to settle for a few minutes. This assay revealed that the cytosolic domain could not directly bind to microtubules (Fig. 5F) as there was no colocalization between the microtubules and GFP signal from the protein. While the IF images of NOMO-TMCYT colocalizing with MT is what generated the MT binding hypothesis, it is technically challenging to design an *in vitro* MT binding experiment with detergent present in the buffer, which is why the construct without the TM was used. It could be that the TM may be necessary to observe the MT interaction *in vitro*.

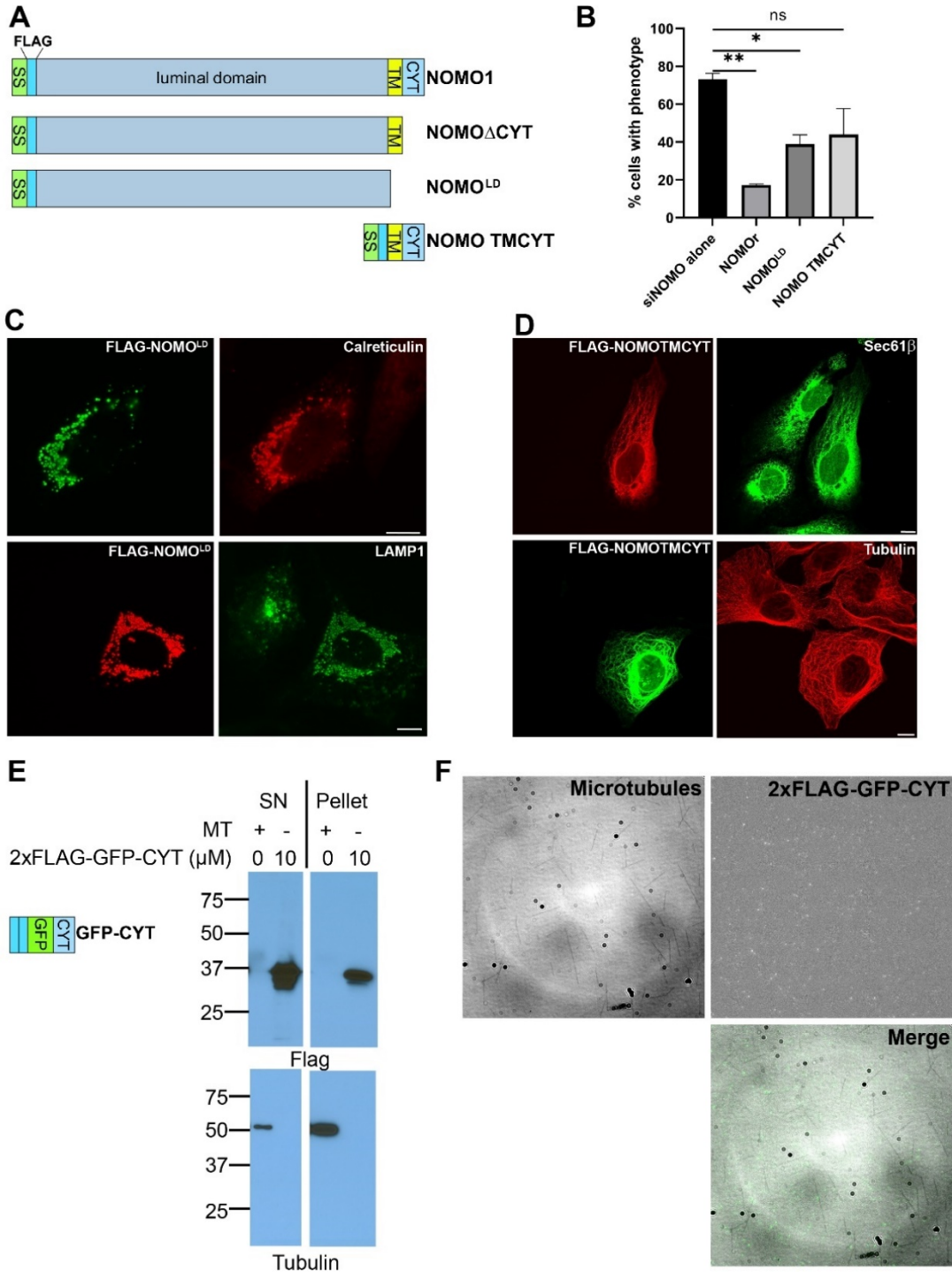


Figure 5. Morphological effects of NOMO domains.

A. Design of the NOMO constructs of varying domains. B. Rescue assay of the NOMO constructs from A. C. Expression of FLAG-NOMO^{LD} in U2OS cells. D. Expression of FLAG-NOMOTMCYT in U2OS cells. E. Microtubule pelleting assay using 2xFLAG-GFP-CYT. Insert depicts the design of this construct. The two blue rectangles represent FLAG tags as in A. F. TIRF assay using 2xFLAG-GFP-CYT. All scale bars are 10 μm.

NOMO does not affect the GTPase rate of Atlastin2

Due to the reciprocal genetic complementation of NOMO and AtI2 on the hole phenotypes when depleting either NOMO or AtI2, we wondered if NOMO could affect the GTPase rate of Atlastin2. AtI2-FLAG and NOMO1-FLAG were independently expressed and purified from Expi293F cells. Selected fractions were run on an SDS-page gel and stained with Coomassie Blue and the final eluted fractions had no significant contaminating proteins (Fig. 6A). The purified proteins were then used to perform a Malachite Green Assay to measure the GTPase rate of Atlastin2 with or without NOMO. Increasing concentrations of NOMO were used to determine if the increasing ratio of NOMO to AtI2 would have any effect of the GTPase rate of AtI2. NOMO did not significantly affect the GTPase rate of AtI2 in any sample (Fig. 6B). The Malachite Green Assay showed 4 μM phosphate released over 4 hours, which agrees with the literature value of the AtI2 GTPase rate (Morin-Leisk et al., 2011; Moss et al., 2011).

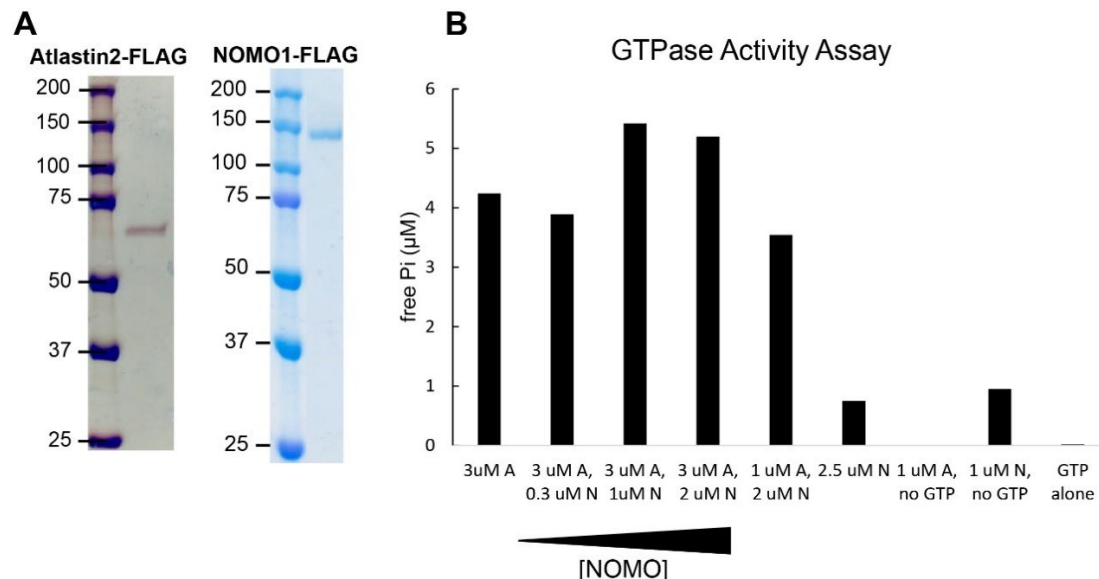


Figure 6. NOMO does not affect the AtI2 GTPase rate.

A. Representative fractions of the respective purified proteins selected for the Malachite Green assay. B. Results of the Malachite Green Assays to measure the GTPase rate of AtI2. Data shown is the average of three assays. A is used to abbreviate AtI2-FLAG, N is used to abbreviate NOMO1-FLAG.

Microtubules are excluded from the holes under NOMO depletion

Due to the importance of ER-MT interactions and the observed NOMO-TMICYT phenotype that colocalizes MT to the ER, I wondered what the localization of MT would be under NOMO depletion. To understand this, I depleted U2OS cells of NOMO. I then used nocodazole to cause the depolymerization of MT and observe how the MT localization would be affected. A set of siControl samples were also analogously treated with nocodazole for the indicated lengths of time (Fig. 7A). In the control cell samples, as the time of the nocodazole treatment increase, the tubulin became less organized and was generally enriched around the nucleus where the ER had also condensed to. In the NOMO depleted samples, a similar trend can be seen, but tubulin is completely excluded from the visible holes.

Tubulin also appears to be enriched around the holes from NOMO depleted samples under nocodazole treatment. This could indicate that if an organelle resides in the hole, this unidentified resident does not have significant attachment to microtubules. These enriched areas of tubulin could also indicate acetylated MT as acetylated MT are known to be more resistant to nocodazole treatment (Friedman et al., 2010). Acetylated MTs are enriched at sites of ER sliding (Friedman et al., 2010). An observable enrichment of acetylated MT around the holes could be indicative of increased mobility around these holes, possibly indicating that a higher rate of rearrangement is necessary to maintain the ER network. This hypothesis could be tested via live cell imaging.

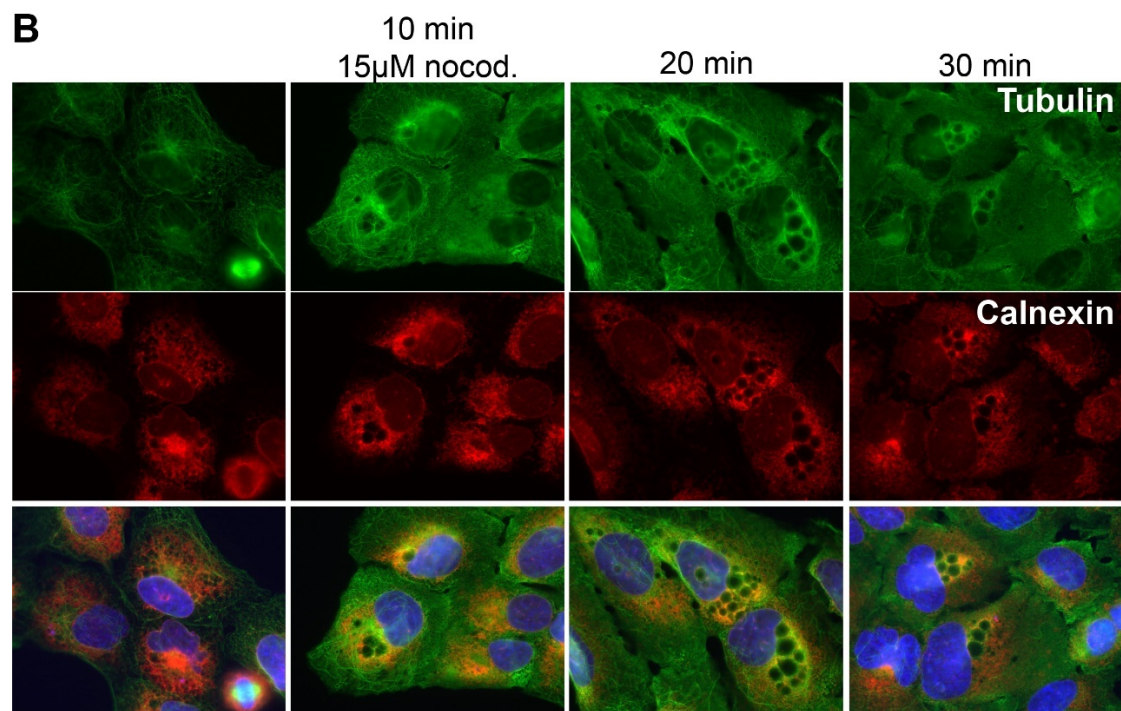
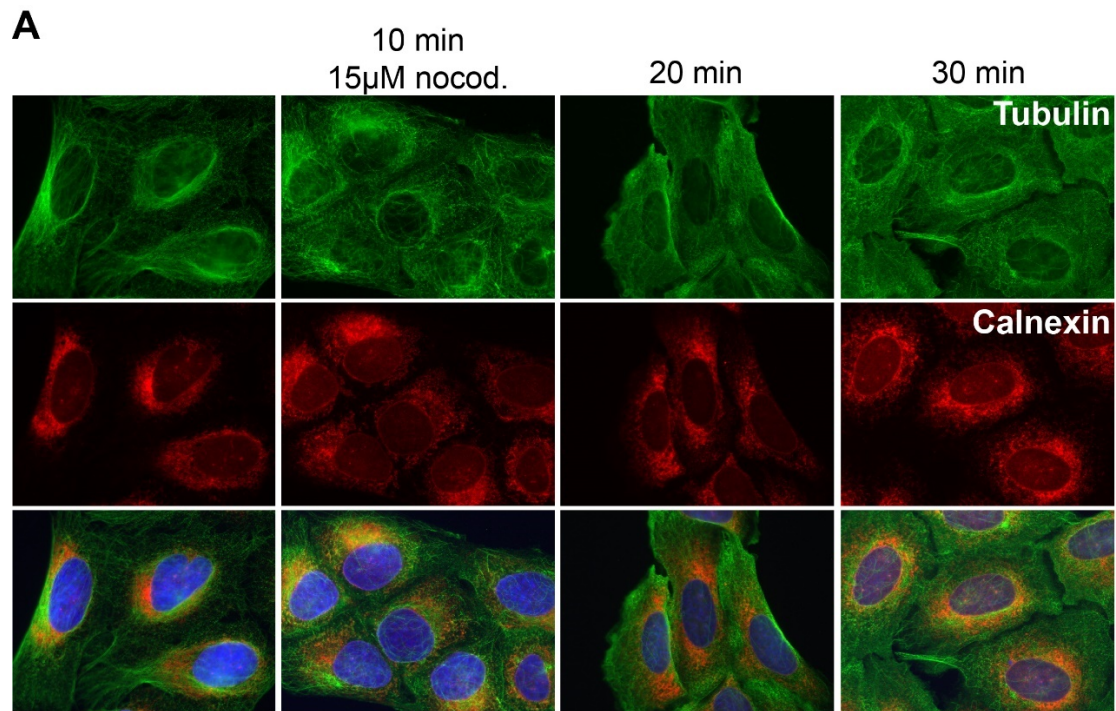


Figure 7. Tubulin is excluded from NOMO depletion holes.

A. U2OS cells treated with siControl and treated with 15 μ M nocodazole for the indicated length of time. B. U2OS cells treated with siNOMO and treated with 15 μ M nocodazole for the indicated length of time. Tubulin is used as the MT marker, calnexin is used as the ER marker.

Lipid levels under NOMO depletion

Because the holes under NOMO depletion were circular, we initially wondered if lipid droplets were localizing to the holes, and if there was a change in lipid levels. Therefore, control and NOMO depleted samples were processed for immunofluorescence. Samples for each condition were also fed with oleic acid (OA) as a positive control for lipid droplet visualization as IF sample processing can cause the loss of lipid droplets if not performed properly. BODIPY (493/503) was used to visualize the lipid droplets. Control cells that were not fed with OA had no BODIPY signal while the fed sample had strong signal and lipid droplets were visible (Fig. 8A). NOMO depleted samples that were not fed with OA did have a BODIPY signal near and around the holes, but the fluorescence signal was low. The fed sample again had strong signal allowing validation that the proper IF method was followed which appeared much like the control sample (Fig. 8A).

To quantitatively determine if specific lipid levels were affected, a control sample and a NOMO depleted sample were submitted for lipid analysis. A rescue sample co-transfected with siNOMO and NOMO1r-FLAG was also submitted for comparison. The most notable difference was a decrease in phosphatidylcholine (PC) from 62% of the total lipids in control cells to 47% in NOMO depleted cells, with the rescue construct bringing the level up to 53% of the total lipids (Fig. 8B). Cholesterol esters (CE) also appeared slightly higher, from 1% of the total lipids in control cells to 3.5% in NOMO depleted cells, which might explain the visible lipid droplets by IF under NOMO depletion compared to control (Fig. 8A,B). A decrease in PC production is known to cause accumulation of lipid

droplets (Testerink et al., 2009). This may explain why we were able to observe lipid droplets under NOMO depletion without OA.

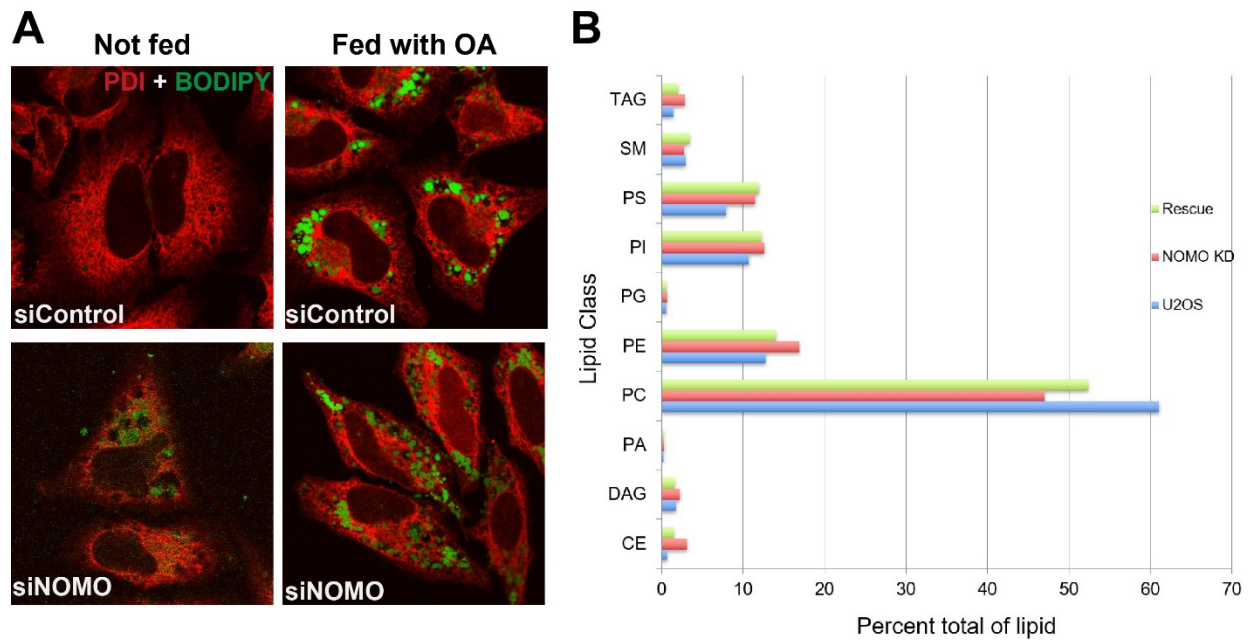


Figure 8. Lipid levels under NOMO depletion.

A. U2OS control or NOMO depleted cells, not fed or fed with OA. PDI is used as an ER marker, BODIPY is used to dye lipid droplets. B. Lipid analysis of control, NOMO depleted, and rescue treated U2OS cells.

Ultrastructural and compositional characterization of hole phenotype

To further explore the relationship between holes and the ER membrane, we processed U2OS cells depleted of NOMO for transmission electron microscopy (TEM). The holes were of significant size with an average area of about 1.2 μm^2 (Fig. 9A, C). Furthermore, holes often appeared to be devoid of any internal electron density and were delineated by membranes in various instances. In general, we encountered fixation issues resulting in suboptimal preservation of holes, possibly due to their large size and low interior content. While these fixation issues generally complicated direct visualization of membrane continuity, in several cases we observed that multiple membranes surrounded one hole (Fig. 9A, bottom panel). For comparison, we performed TEM

analysis of U2OS cells under AtI2 depletion and observed similar membrane delineated holes (Fig. 9B). The area of the holes under NOMO depletion and Altastin2 depletion were not significantly different (Fig. 9C). These results support the idea that a similar net result is obtained in response to the depletion of either NOMO or AtI2. Lastly, we noted electron-dense structures adjacent to or inside a subset of the holes under NOMO depletion that could be lysosome or phagosome organelles (Fig. 9A, top and middle panels).

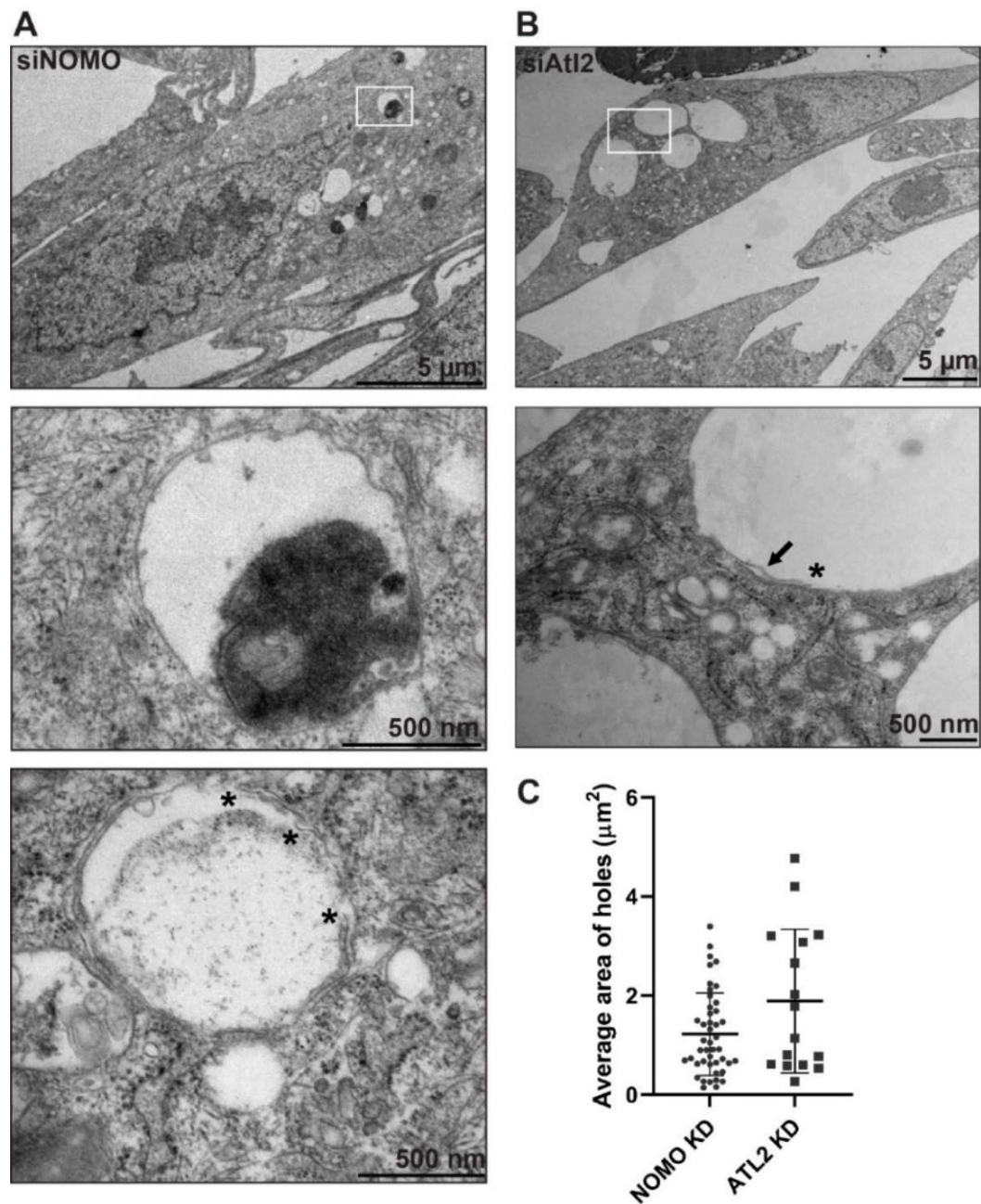


Figure 9. EM analysis of NOMO and AtI2-depleted cells.

A. U2OS cells were successively treated with two doses of siNOMO 24 hrs apart and fixed 48 hrs after the second dose for EM processing. White square in the top panel identifies selection for middle panel. Asterisks in bottom panel denote free membrane ends. B. U2OS cells successively treated with two doses of siAtI2 as described in (A). Arrow in second panel indicates an identified membrane outlining the hole. C. Quantification of the area of observed gaps in A and B quantified on ImageJ. Error bars indicate standard deviation.

Three-dimension investigation of observed hole

The imaging data acquired thus far has provided only two-dimensional information on the hole phenotype. We wondered if the observed holes were spherical in nature or cylindrical, as an empty column spanning from the top to the bottom of the cell. Our first approach was to take a z-stack image on the confocal of U2OS cells under NOMO depletion. The z-stack revealed that while the hole does get slightly smaller or larger through some of the imaged planes, the flatness of U2OS cells proves challenging (Fig. 10A). The hole takes on a “pancake-like” shape based on these data. While the hole phenotype was also observable in HeLa cells depleted of NOMO, the ER network is not as extensive, providing suboptimal ER network imaging.

We then moved on to trying super resolution microscopy. We also hoped that this higher resolution imaging technique would be able to determine if both sheets and tubules were still present or if there were a higher percentage of tubules under NOMO depletion. If NOMO is a sheet protein, it could be possible that NOMO depletion causes less sheets to form. A sec61 β -scarlet stable cell line was generated and used for these experiments. While the signal from the sec61B-scarlet proved to be sufficient, we had similar imaging problems as with the confocal images. We were able to better identify threads of ER network at the absolute bottom of where the hole was observed, but the top of the hole was difficult to capture (Fig. 10B). Additionally, the ER was too dense to be able to clearly demarcate all sheet areas from tubules. There were clearly sheet structures present, but we could not make a fair comparison with a wild-type cell due to the ER density. Lastly, we also submitted U2OS cells for EM tomography under high pressure freezing, but high pressure freezing does not preserve ER morphology well (data not shown).

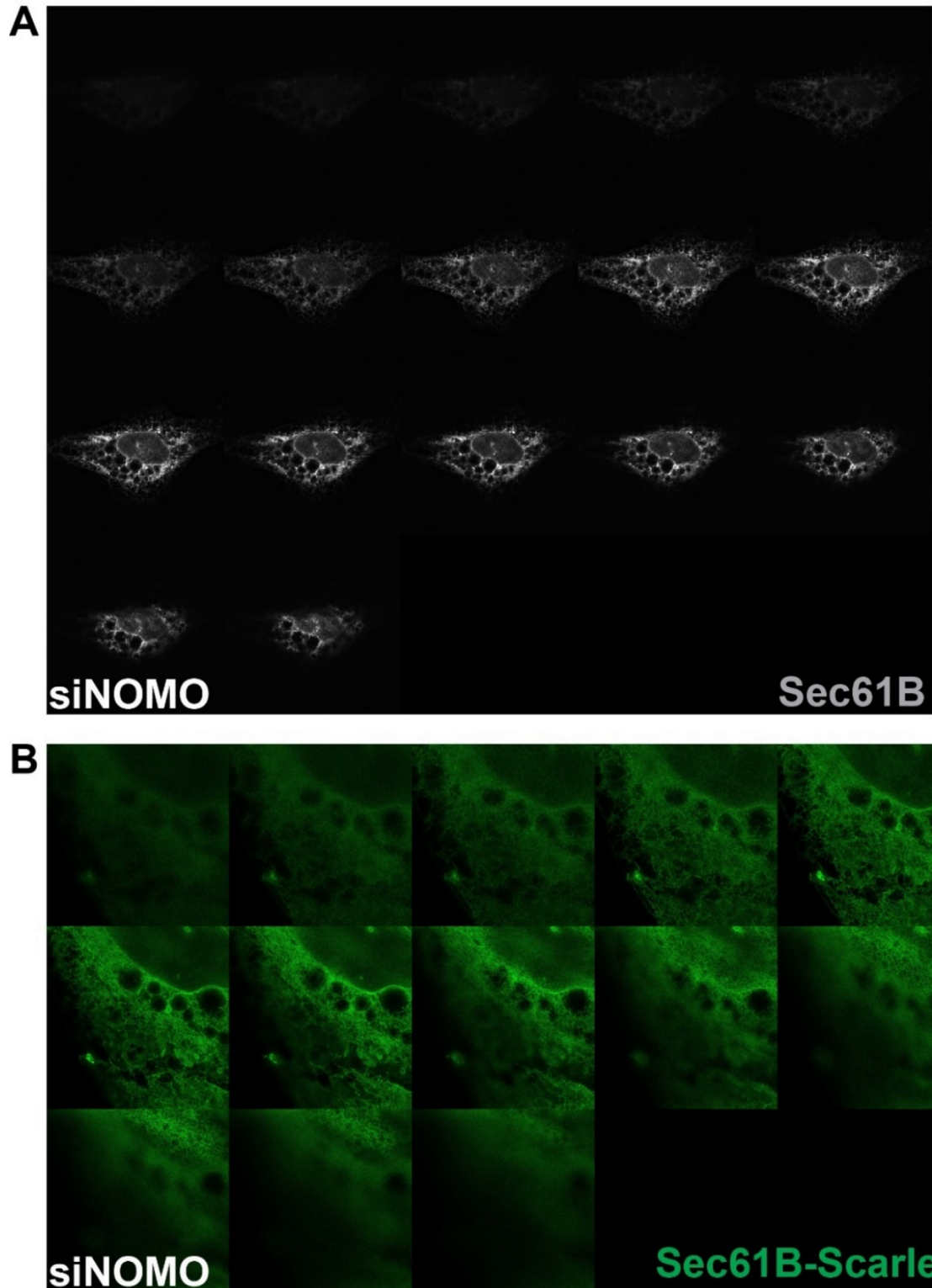


Figure 10. Three-dimensional morphology of the NOMO depletion hole.

A. Z-stack montage of a U2OS cells treated with siNOMO, sec61B is used as the ER marker. B. Super resolution imaging of sec61B-scarlet stable U2OS cells treated with siNOMO.

3.2 NOMO depletion disrupts autophagy

To determine if the observed electron-dense structures by EM (Fig. 9) represent lysosomal compartments, U2OS cells were treated with siNOMO, siAtI2, or siClimp63 and analyzed by immunofluorescence microscopy using a lysosomal-associated protein 1 (LAMP1)-specific antibody. Indeed, we observed a large accumulation of LAMP1 signal in the ER holes resulting from NOMO and AtI2 depletion (Fig. 11A). The observed increase in lysosome size and accumulation compared to control cells could be an indicator of increased autophagy (de Araujo et al., 2020). To address this point, we monitored LC3 processing by immunoblotting. LC3-I is processed to LC3-II as lysosomes increase their autophagic activity (Tanida et al., 2008). LC3-II is substrate of the autophagy pathway, therefore, LC3-II accumulation can also indicate autophagy inhibition (Yoshii and Mizushima, 2017). I used a Western Blot to probe for LC3 levels and there was a drastic increase of LC3-II under NOMO depletion compared to control, which is indicative of autophagy induction, inhibition, or dysregulation (Fig. 11B). I also monitored LC3 processing under the depletion of ER shaping proteins Climp63 and AtI2, and NOMO binding partners TMEM147 and Nicalin (Dettmer et al., 2010; Haffner et al., 2007). An increase in LC3-II was also observed upon Climp63 depletion, though less pronounced compared to NOMO depletion (Fig. 11B), whereas the other tested conditions did not significantly increase LC3-II levels. Therefore, only Climp63 and NOMO depletions lead to an increase of LC3-II, indicative of autophagy induction or dysregulation. We did not observe an increase in BiP levels under NOMO depletion, which would have indicated an induction of the unfolded protein responses (UPR) due to ER stress (Fig. 11C) (Walter and Ron, 2011).

To distinguish between autophagy induction or inhibition, I first treated the cell samples with Bafilomycin A (Baf A) for four hours to inhibit autophagy (Yoshii and Mizushima, 2017). and observed the increase in LC3-II levels upon this autophagy inhibition. While siControl, siClimp63, and siAtf2 demonstrated an increase in LC3-II levels with the addition of Baf A, siNOMO LC3-II levels were already close to saturation without Baf A treatment (Fig. 11C). I then immunoblotted to determine the levels of p62 under NOMO depletion, which were also very increased under NOMO depletion compared to control (Fig 11D). P62 is degraded by the autophagy pathway, therefore accumulation of p62 is used to measure the inhibition of autophagy when paired with a Baf A assay (Yoshii and Mizushima, 2017). The accumulated level of p62 under Baf A treatment compared to control represents the p62 that should have been degraded during the time the Baf A treatment took place (Yoshii and Mizushima, 2017). When quantified, NOMO depleted cells have already accumulated the level of p62 as a control sample treated with Baf A, but further accumulate p62 when treated with Baf A. This additional p62 increase above siControl p62 levels is not common. This likely represents an increase in autophagic flux and inhibition of autophagy. Climp63 depleted cells also demonstrated p62 levels at saturation levels compared to the control sample with and without Baf A treatment. This is the first indication that Climp63 depletion can disrupt an associated ER function.

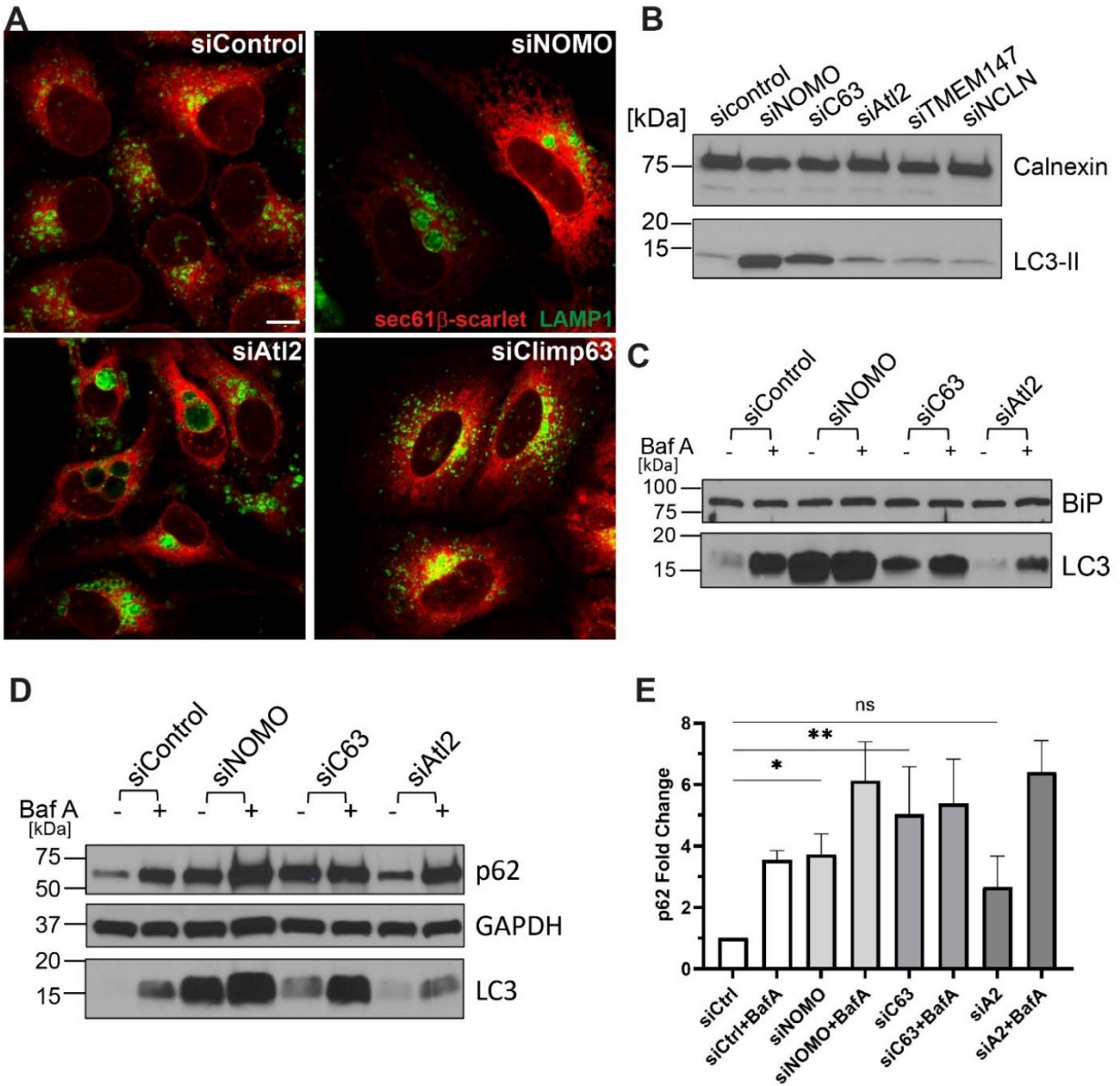


Figure 11. Sheet disruption inhibits autophagy.

A. Representative images of U2OS cells treated with the respective siRNA to identify lysosome localization using LAMP1 as a marker. Scale bar is 10 μ m. B. Immunoblot with calnexin and LC3 antibodies using U2OS cells extracts treated with the indicated siRNA. C. Immunoblot with BiP and LC3 antibodies of the Baf A treated samples under the respective siRNA conditions. D. Immunoblot using p62, GAPDH, and LC3 antibodies of the Baf A treated samples under the respective siRNA conditions. E. Quantification of the fold change in p62 levels, calculated by dividing p62 intensity by GAPDH intensity and comparing to the undertreated control sample. One asterisk means $P < 0.05$, two asterisks means $P < 0.01$.

3.3 Structural characterization of NOMO1

NOMO1 overexpression imposes ER sheet morphology

We hypothesized that if NOMO could contribute to ER intermembrane spacing, then overexpressing NOMO1 should affect the spacing of the ER lumen as Climp63 does (Shen et al., 2019). To first determine that NOMO is enriched in ER sheets, we overexpressed FLAG-NOMO1 in U2OS cells and imaged cells using PDI as the ER marker. Representative images have been selected to demonstrate that at low expression levels, FLAG-NOMO1 shows normal ER morphology. As the expression of FLAG-NOMO1 increases, there is an increase in continual ER areas reminiscent of sheets by confocal microscopy compared to the shorter structures of untransfected cells (Fig. 12A).

To determine if ER sheet spacing was affected, we prepared HeLa cells overexpressing FLAG-NOMO1, as well as control cells transfected with empty vector, for thin-slice electron microscopy imaging. Cells overexpressing FLAG-NOMO1 had a constricted ER lumen diameter compared to control cells (Fig. 12C, D). When quantified, FLAG-NOMO1 overexpression reduced the diameter of the ER lumen from an average intermembrane space of 64 nm to 33 nm (Fig. 12E). Interestingly, a similar reduction in ER lumen diameter results from depleting Climp63, where the ER lumen is decreased to a diameter of 30 nm (Shibata et al., 2010), potentially suggesting that NOMO could have a role in maintaining this smaller intermembrane space.

If NOMO could be the remaining ER sheet spacer, we reasoned that simultaneous depletion of NOMO and Climp63 would result in a synthetic effect. Would the ER intermembrane space become wider than in a wild-type cell? The intermembrane space could alternatively decrease as sheet shaping proteins have been proposed to help keep

the opposing sheet membranes from collapsing into each other (Schweitzer et al., 2015). To address this question, we simultaneously depleted U2OS of NOMO and Climp63 and processed the cells for electron microscopy. The ER lumen was restricted to an average diameter of 40 nm (Fig. 12E), which was statistically significantly less than the control sample of 64 nm. This result does not fit either hypothesis and suggests that ER sheet morphology is not dependent on these two proteins alone.

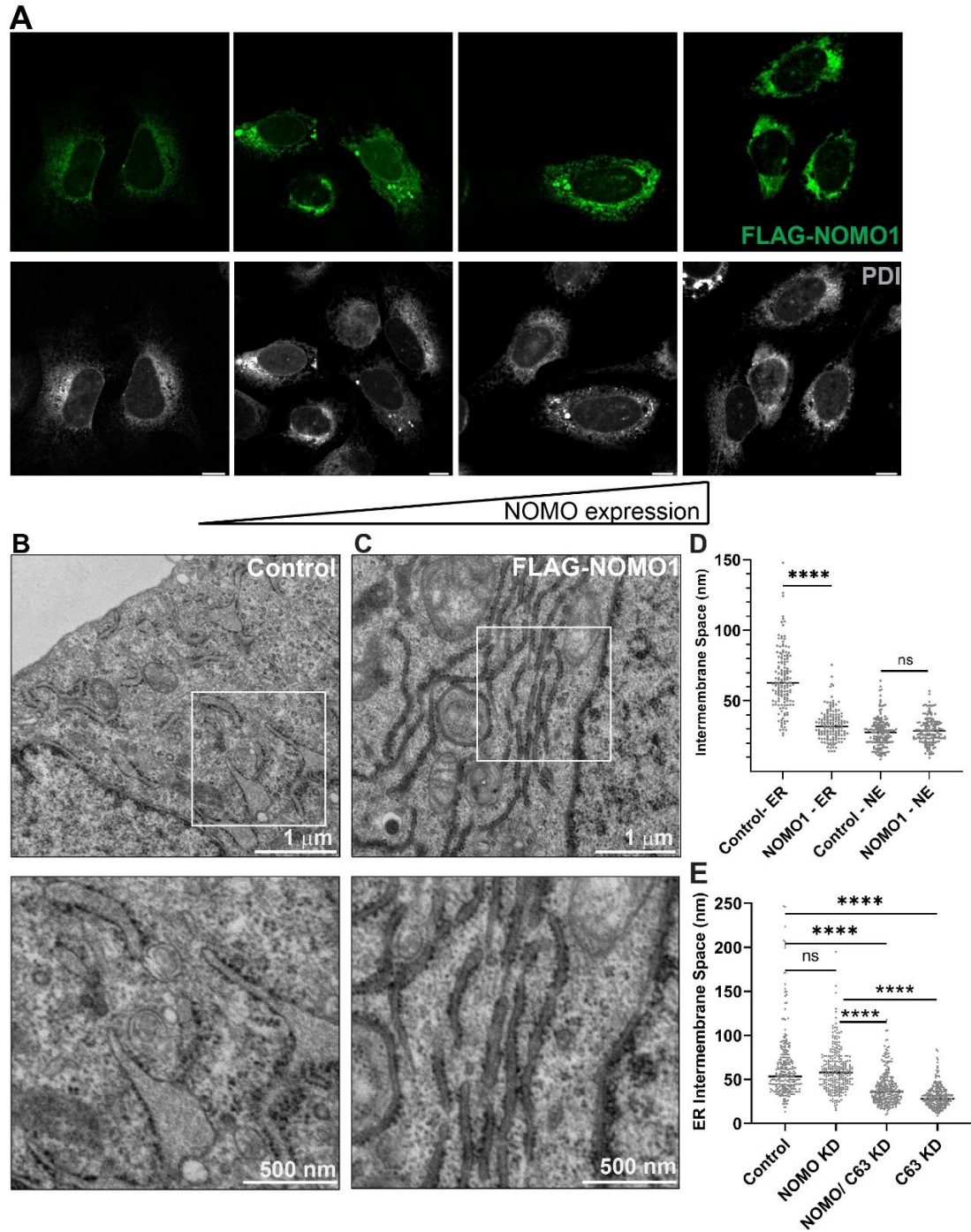


Figure 12. NOMO1 restricts the ER lumen.

A. Increasing expression of FLAG-NOMO1 with ER marker, PDI, in U2OS cells. B. HeLa cells transfected with empty vector pcDNA3 as a control. White box identifies selected zoomed area in bottom panel. C. HeLa cells transfected with FLAG-NOMO1. White box identifies selected zoomed area in bottom panel D. Quantified diameters of ER and NE HeLa cell cross sections from A and B. E. Quantified diameters of U2OS ER and NE cross sections of U2OS cells treated with the respective siRNAs. Four asterisks indicate $P < 0.0001$, ns = not significant.

NOMO is a rod-shaped dimer

Since the overexpression of NOMO causes a uniform restriction of ER intermembrane spacing, we hypothesized that NOMO may support sheet structure by dimerizing across the sheet membranes to support the luminal diameter as originally proposed for Climp63 (Shibata et al., 2010). To determine if NOMO could oligomerize, NOMO1-FLAG was purified from Expi293F cells and analyzed by size exclusion chromatography (Fig. 13A). NOMO1-FLAG eluted at an apparent mass of about 500 kDa based on elution position, which would correspond to a tetramer of NOMO1. However, the potentially elongated form and the correspondingly large apparent Stokes radius of NOMO1 could be contributing to an experimental error.

To more accurately determine the oligomeric state and molecular mass of NOMO1-FLAG, we used size-exclusion chromatography coupled to multiple angle light scattering (SEC-MALS). The SEC-MALS analysis revealed a radius of gyration (R_g) of about 15 nm (Fig. 13B) corresponding to the main peak in the elution profile. Reconstitution of membrane proteins using detergents often leads to the formation of 'protein detergent complexes' (PDCs) and therefore, we performed a protein conjugate analysis on this peak to delineate the molar mass of the protein component from the total molar mass of the PDC. According to this analysis, the molar mass of NOMO1 ranged from ~270 kDa on the left side of the peak to ~230 kDa towards the right side of the peak, with each value representing the mass after correction for detergent contribution (Fig. 13B). This apparent polydispersity across the peak is not uncommon for oligomeric membrane proteins reconstituted in the presence of detergents (Albright et al., 2006; Slotboom et al., 2008; Veessler et al., 2009). Based on the observed mass range, we

suggest that NOMO1 forms a low-affinity dimer, however additional equilibrium methods will be required to definitively determine the oligomeric state.

To avoid complications arising from the detergent micelle, we also performed SEC-MALS analysis with a NOMOLD-FLAG construct (128 kDa) lacking both the TM domain and the CYT domains. After a protein conjugate analysis, the monodisperse peak correlated to a mass of 142 kDa, consistent with NOMOLD-FLAG being a monomer (Fig. 13C). Furthermore, NOMOLD-FLAG had a similar R_g (~14 nm) as full-length NOMO1-FLAG. These data argue in favor of full-length NOMO forming a potential parallel dimer, but as mentioned before, additional experiments will be required to rigorously test this proposal in the future.

Given that the luminal domain was not sufficient for oligomerization, we tested if NOMO could dimerize via the transmembrane (TM) and cytosolic tail (CYT) domains. To this end, the TM-CYT domains were fused to maltose binding protein (MBP) to yield 2xFLAG-MBP-TM-CYT, which was expressed, purified from Expi293F cells and subjected to SEC-MALS analysis. The molar mass of the MBP-TM-CYT peak was estimated to be ~120 kDa from SEC-MALS. However, protein conjugate analysis revealed that the molar mass of MBP-TM-CYT is 58 kDa and the detergent contributed 62 kDa to the apparent molar mass of the PDC, revealing that MBP-TM-CYT is a monomer (Fig. 13D). At this point, we cannot rule out that MBP sterically interferes with a possible dimerization, or that several distinct structural features in NOMO1 contribute to dimerization collectively but are insufficient to confer dimerization individually.

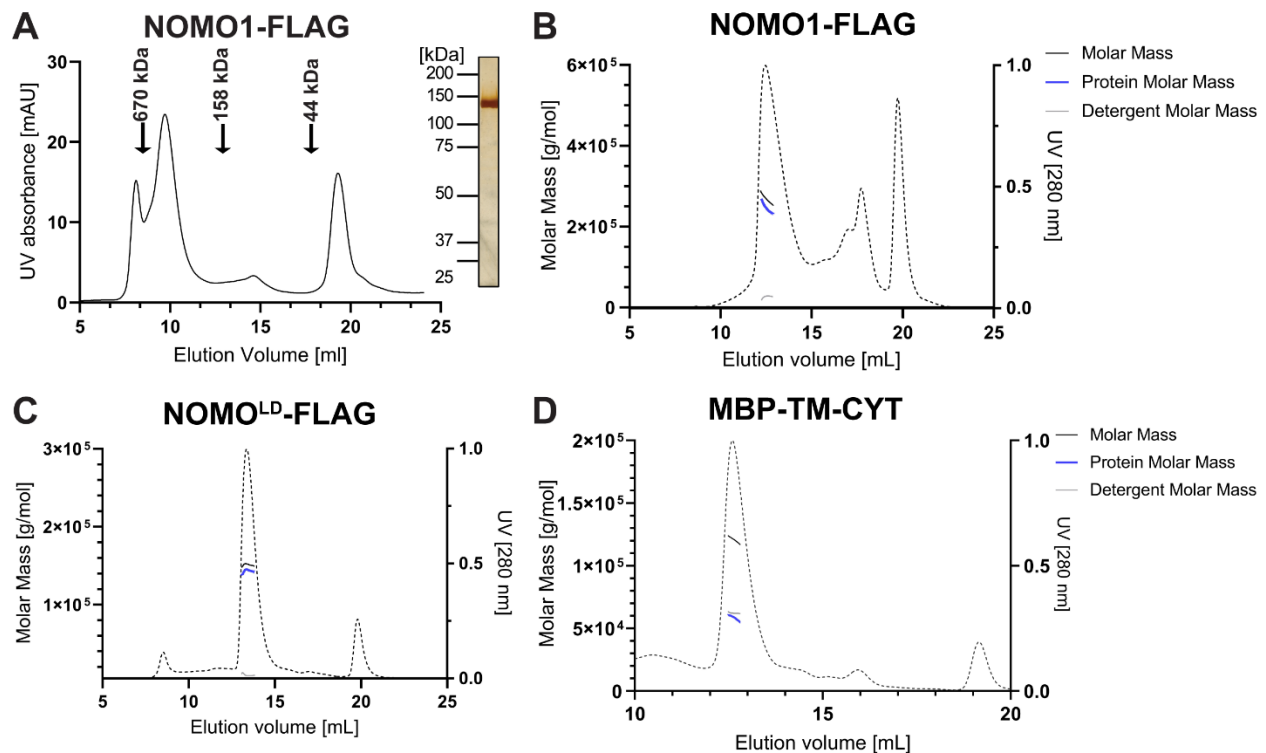


Figure 13. Determination of the NOMO1 oligomeric state.

A. Elution profile of NOMO1-FLAG on a S200 column. Insert: SDS-PAGE/silver stain of NOMO1-FLAG fraction obtained from preparative SEC. B. In-line SEC-MALS profile of NOMO1-FLAG subjected to a Superose 6 column. Dashed line is the UV trace, Molar Mass represents the total molar mass of the PDC, Protein Molar Mass is the corrected molar mass to remove contribution of detergent. C. SEC-MALS profile of NOMOLD-FLAG subjected to a Superose 6 column; lines as defined in B. D. In-line SEC-MALS analysis of MBP-TM-CYT subjected to a S200 Increase column.

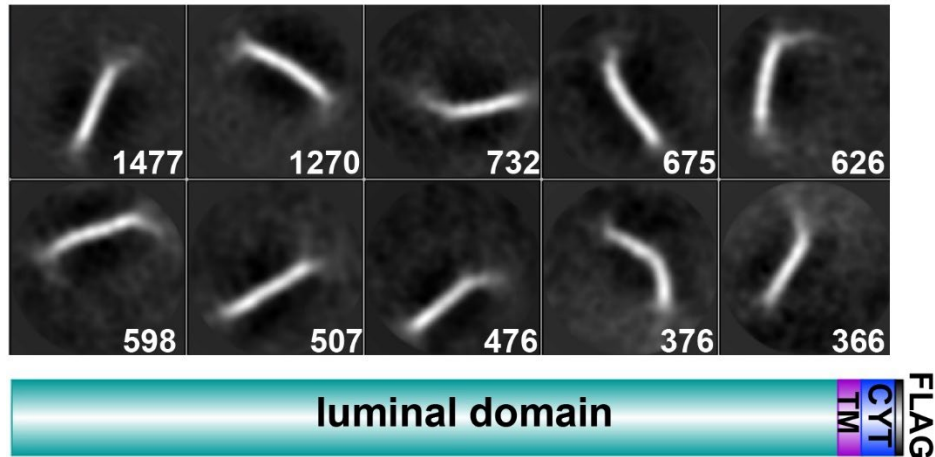
NOMO1 adopts a “beads on a string” morphology

As a first step towards a better structural understanding of NOMO1, we set out to determine the overall architecture of the molecule. NOMO1-FLAG was purified from Expi293F cells and the sample was analyzed by negative-stain EM. 2D class averages were generated using RELION from 7,000 particles. The top 2D class averages from the collected data set feature a flexible, extended rod of about 30 nm (Fig. 14A). A 3D model was modeled from this data and is 27 nm in length (Fig. 14B), which is similar to the 33 nm ER intermembrane space measured by EM under NOMO overexpression (Fig. 12E).

Crystallography attempts were also made with NOMO1-FLAG purified without detergent and were all unsuccessful due to the need for 0.05% n-Dodecyl-B-D-Maltoside (DDM) to prevent NOMO1-FLAG from crashing out of solution. Bacterial expression and purification of several NOMO constructs in various bacteria strains were also attempted to increase the protein yield. These were unsuccessful due to degradation of the NOMO protein.

To determine if a NOMO monomer alone would be similar in length as suggested by the SEC-MALS data and the cytosolic dimerization domain, a negative stain structure was also determined for NOMO^{LD}-FLAG since this construct is a monomer. NOMO^{LD}-FLAG was purified from Expi293F cells and visualized by negative-stain EM. The 2D classifications were generated using RELION from 9,000 particles and revealed a flexible, slightly thinner rod-shaped molecule compared to the full-length protein. Interestingly, the class averages feature a “beads on a string” morphology with eight discernable globular segments (Fig. 14C), probably accounting for Ig-like domains given the structural homology to Ig-fold proteins. The obtained 3D model is about 24 nm in length. In conclusion, NOMO1 is a flexible, rod-shaped parallel dimer featuring a “beads on a string” arrangement of eight consecutive domains, most of these domains, if not all, may represent Ig-like folds.

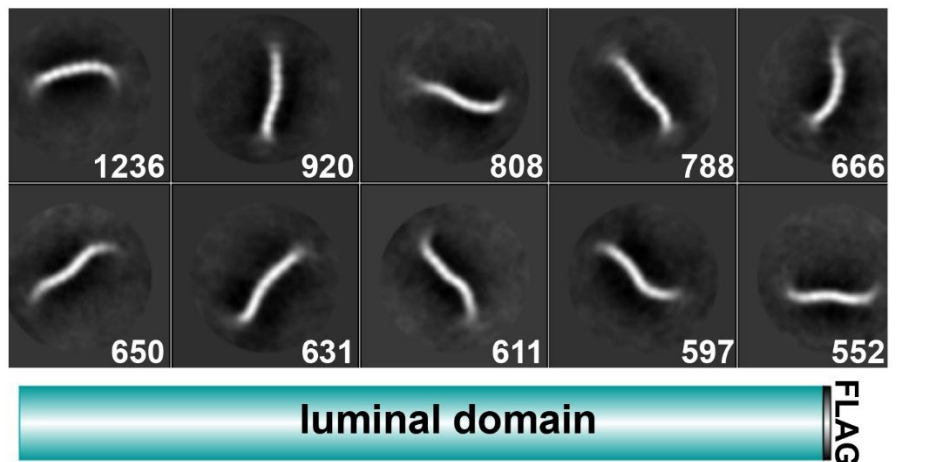
A NOMO1-FLAG



B



C NOMO^{LD}-FLAG



D



Figure 14. Single particle analysis of NOMO1.

A. Top 10 2D class averages of ~7,000 picked negative stain NOMO1-FLAG particles, numbers of particles per class in square. Mask diameter is 40 nm. A construct layout is inserted to clarify protein domains; TM, transmembrane domain, CYT, cytosolic tail. B. 3D reconstruction from A, scale bar is 10 nm. C. Top 10 2D class averages of ~10,000 picked negative stain NOMO Δ TM-FLAG particles, number of particles per class in square. Mask diameter is 30 nm. A construct layout is inserted. D. 3D reconstruction from C, scale bar is 10 nm.

Due to the high degree of symmetry of a NOMO molecule, it was not possible to distinguish the N-terminal end from the C-terminal end. If we could distinguish the two ends, we hoped it would increase the possibility of clearly identifying the dimer species of full-length NOMO. The first approach I took to overcome this ambiguity was to purify NOMO1-FLAG and then incubate the purified protein with FLAG (M2) antibody. I then ran the mixture through a size exclusion column to select for fractions of higher apparent molecular mass than NOMO1-FLAG alone, which should represent samples of NOMO1-FLAG with FLAG antibody bound to it. Fractions that were of higher molecular mass than what is expected of NOMO1-FLAG alone were selected for negative stain sample preparation. The resulting top ten 2D classes showed particles of similar lengths to the original NOMO1-FLAG data set as well as a few shorter in length classes, which may represent the FLAG antibody alone (Fig. 15A).

The next approach to distinguish the C-terminal end was to design a construct with MBP at the C-terminal end, NOMO1-MBP-FLAG. The top eight classes showed that the addition of MBP was not significant enough to distinguish the C-terminal end as the classes were similar to the NOMO1-FLAG and NOMO^{LD}-FLAG class averages (Fig. 15B). The inherent flexibility is likely what is contributing to the ambiguity of the ends of the molecule. These particles had an average length of 25 nm. There were two lower populated classes that could possibly represent dimers, but the low population does not allow for modeling.

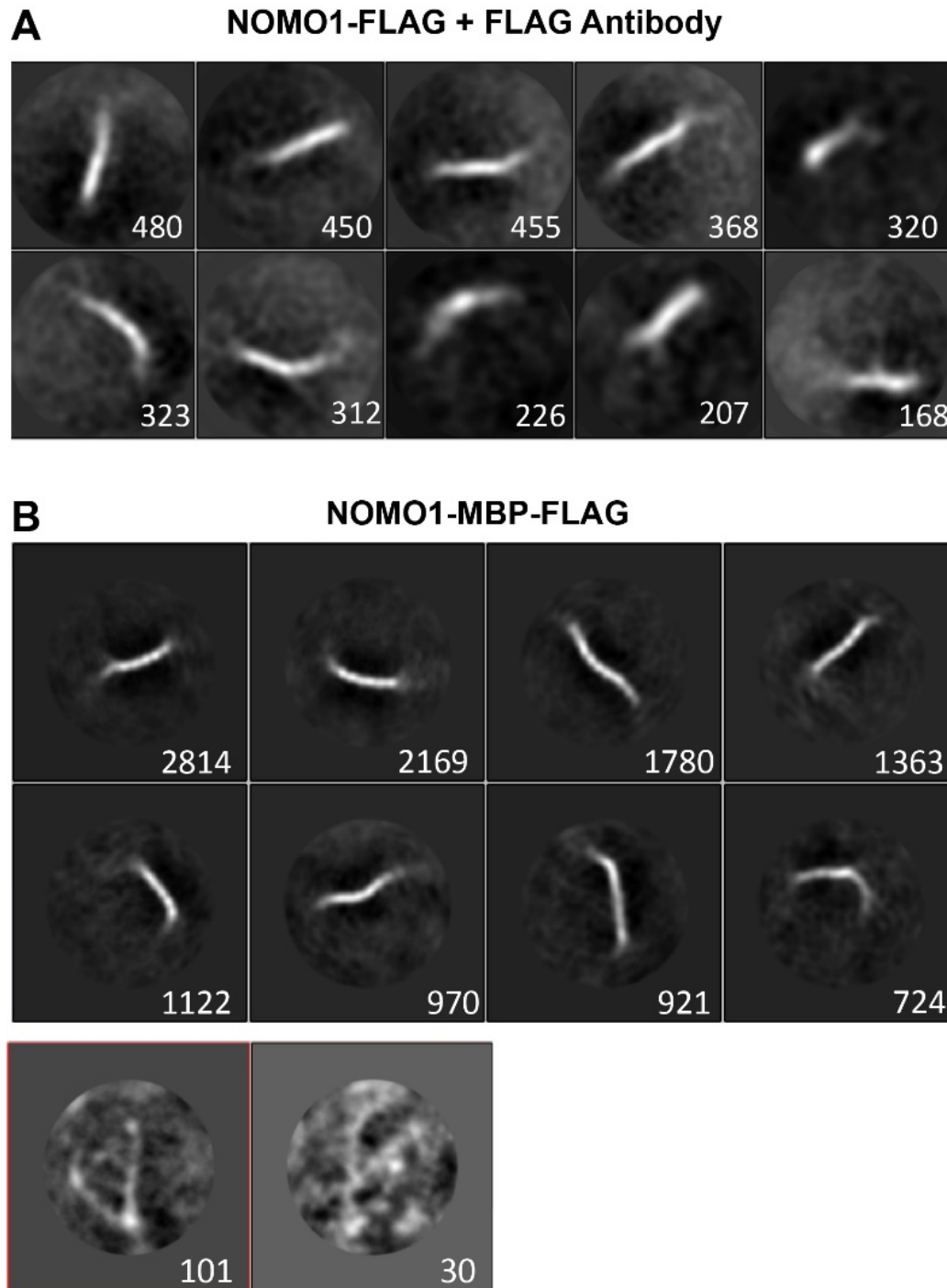


Figure 15. The flexibility of NOMO prevents distinguishing the C-terminal end.

A. Top ten 2D classes of NOMO1-FLAG incubated with FLAG antibody. Mask diameter is 30 nm. The white numbers represent the population of each class. B. Top eight 2D classes of NOMO1-MBP-FLAG and two additional lower populated classes. Mask diameter is 40 nm. The white numbers represent the population of each class.

NOMO dimensions and ER intermembrane spacing

To definitively show that the length of NOMO will affect the ER intermembrane space, two longer NOMO constructs were designed. The first construct, 2lumen-NOMO1-FLAG has the NOMO luminal domain duplicated, which should produce a 268 kDa protein and have an approximate lumen length of 52 nm. The second construct, 2xCD4-NOMO1-FLAG, has 2 copies of 4 Ig-fold domains of the human T-cell surface glycoprotein CD4(Choudhuri et al., 2005). This approach was previously used to elongate a single-chain trimer ectodomain involved in T-cell triggering to observe an increase in the intermembrane space of the cell-to-cell interface (Choudhuri et al., 2005). Two copies of the 4 Ig folds have a length of ~20-24 nm, therefore 2xCD4-NOMO1 produces a 221 kDa protein with a potential length of 47-51 nm.

The expression and localization of the constructs to the ER were verified by immunoblotting and immunofluorescence (Fig. 16B,C). The constructs were then transfected into HeLa cells and submitted for thin-section EM processing. The ER lumen did appear thicker in the EM images (Fig. 16D). The quantification of the intermembrane distance revealed that there was a correlative increase with the extended constructs (Fig. 16E). 2xCD4-NOMO1-FLAG increased the average intermembrane distance to 41 nm, a 1.2-fold increase from the 33 nm NOMO1 alone imposes, while 2xlumen-NOMO1 resulted in an average intermembrane distance of 47 nm, a 1.4-fold increase in the intermembrane space.

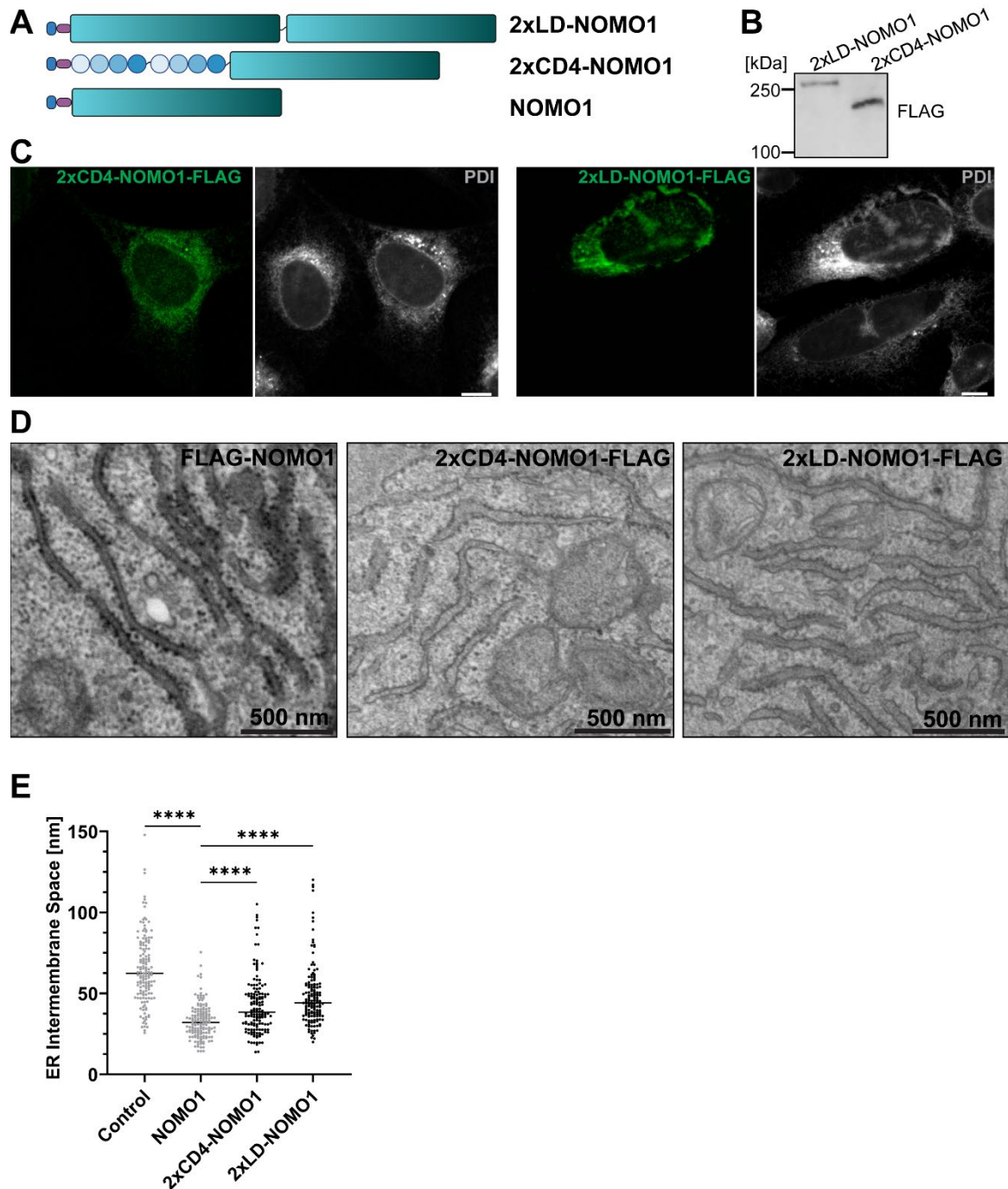


Figure 16. Extended NOMO constructs correlatively increase the intermembrane space. A. Design of the two extended constructs. B. Validation of ER localization by immunoblotting. C. Validation of localization by immunofluorescence. D. Representative EM images of HeLa cells expressing the respective construct. E. Quantification of the ER intermembrane distance of each construct compared to NOMO1-FLAG and control cells. Four asterisks indicate $P < 0.0001$.

3.4 Investigating the role of NOMO in ER-phagy and the Nuclear Envelope

NOMO1 is not likely to have a role in ER-phagy

Due to the observation that NOMO depletion causes enlarged lysosomes and NOMO^{LD} localizes to the lysosomes and ER, we wondered if NOMO could be cleaved by an unknown mechanism to allow NOMO to localize to the lysosomes under ER stress. To induce ER stress, cells transfected with FLAG-NOMO1 or NOMO1-FLAG were treated with either tunicamycin (TN) or thapsigargin (TG) overnight. Samples were then lysed and used for immunoblotting with a FLAG antibody. Both N-terminal and C-terminal FLAG tagged NOMO1 were used to make sure that in case the C-terminal cytosolic tail was cleaved, we would be able to observe a large fragment with the N-terminally FLAG tagged construct. The only difference in mass seen was under tunicamycin treatment, which was expected as TN inhibits glycosylation and NOMO1 is a glycosylated protein (Fig. 17A). To determine if NOMO1 is truly a glycosylated protein, purified NOMO1-FLAG was treated with either PNGase F or Endo Hf, enzymes which are capable of cleaving N-linked oligosaccharides from proteins, and the samples were run on a SDS PAGE gel to determine if there was an observable decrease in the mass. Indeed, both PNGase F and Endo Hf treatment caused an observable decrease in the mass of NOMO1-FLAG (Fig. 17B). NOMO1 has four potential N-linked glycosylation sites. Each glycosylation site is a potential 2.5 kDa, which means a potential difference of 10 kDa between the fully glycosylated and deglycosylated protein.

ER resident proteins that play a role in ER-phagy are known to colocalize with lysosomes upon ER stress. To determine if NOMO localizes to lysosomes under ER stress, U2OS cells transfected with FLAG-NOMO1 were treated with thapsigargin or

tunicamycin overnight. Baf A treatment was also used due to the previous autophagy inhibition observations under NOMO depletion. NOMO did not colocalize with lysosomes under any of the tested conditions (Fig. 17C). Under Baf A treatment, I did observe gaps forming in the ER network (Fig. 17C). Baf A inhibits autophagy and this observation that Baf A treatment causes a similar ER morphology change as NOMO depletion continues to support that NOMO depletion also dysregulates autophagy.

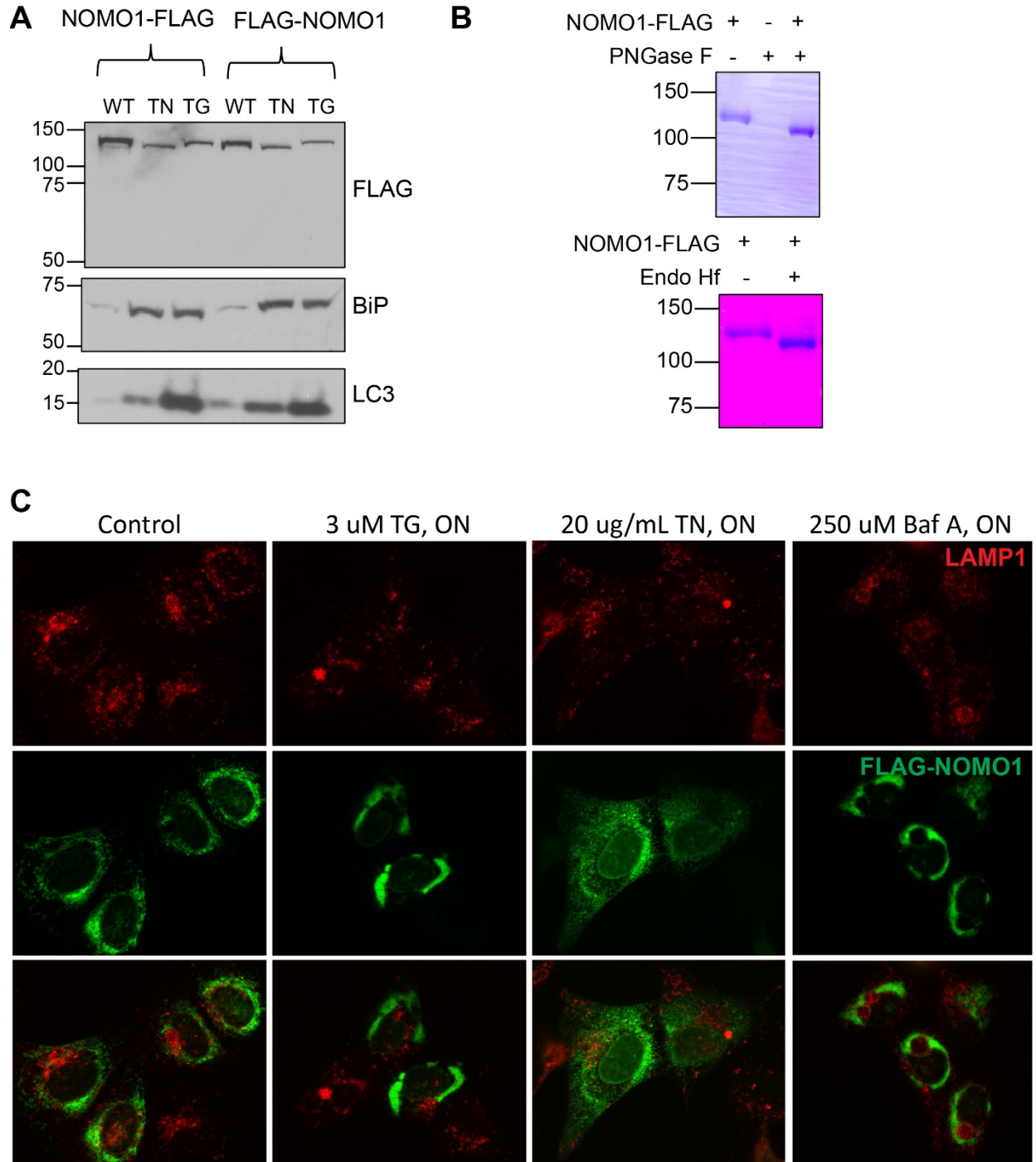


Figure 17. NOMO likely does not have an ER-phagy role.

A. Western Blot of U2OS cell samples treated with chemical ER stressor tunicamycin (TN) and thapsigargin (TG). FLAG antibody was used to detect NOMO. BiP and LC3 were used as ER stress markers. B. Coomassie blue gel of NOMO1-FLAG purified protein treated with PNGaseF of Endo Hf. C. IF images of U2OS cells transfected with FLAG-NOMO1 treated overnight with the respective conditions. LAMP1 is a lysosome marker.

The potential role of NOMO in the Nuclear Envelope

When we overexpressed FLAG-NOMO1 in HeLa cells, we observed a restricted, uniform diameter of the ER intermembrane space, but we also observed that the ER lumen and nuclear envelope were of a darker density than the wild-type control (Fig. 12). This led us to hypothesize that NOMO1-FLAG could localize to the nuclear envelope. To test this idea, a dox-inducible NOMO1-FLAG stable cell line was generated in U2OS. This cell line was submitted for immunogold labeling and EM imaging. Indeed, the images showed that NOMO1-FLAG could localize to the ONM and INM (Fig. 18A), although there is a high background of beads in the nucleus. Additionally, overexpression of an ER protein can cause protein mislocalization and additional experiments, such as endogenous tagging via CRISPR, will be required to test this idea going forward.

Although NOMO overexpression or depletion did not affect the NE spacing in U2OS or HeLa cells (Fig. 12D, E), we wondered if the LINC complex could be obstructing any phenotypes NOMO depletion would be causing. Therefore, we used a SUN1/2 KO A459 cell line to determine if there were any significant changes in the NE spacing upon NOMO depletion. We expected to see the NE intermembrane space increase under NOMO depletion in the SUN1/2 KO cell line. When quantified, there was a statistically significant decrease in the spacing under NOMO depletion in the SUN 1/2 KO cell line (Fig. 18B). I then used IF to determine if NOMO depletion could affect the localization of INM protein Lamin B-receptor (LBR) and SUN2 using endogenous antibodies for the respective proteins. SUN2 accumulated in the ER under NOMO depletion compared to the control sample (Fig. 18C). While there appeared to be less SUN2 signal under NOMO depletion, this was not a significant difference observed by Western Blotting compared to

a control sample (data not shown). There was also a significant accumulation of LBR in the ER (Fig. 18C). When probed by Western Blot, NOMO depleted cells showed less LBR than the control (Fig. 18D). One potential mechanism for NOMO depletion causing LBR to accumulate in the ER is that as an ER shaping protein, NOMO depletion is disrupting the connections of the ER to the NE. If this were the mechanism, depleting AtI2 or Climp63 should also cause LBR to accumulate in the ER. Therefore, I depleted U2OS cells of AtI2, Climp63, Elys, a nucleoporin protein required for nuclear pore assembly whose depletion should cause LBR to accumulate in the ER, and NCLN, a NOMO interaction partner. LBR accumulation was only seen under Elys or NOMO depletion, showing specificity to the observed accumulation of LBR in the ER (Fig. 18E). The decrease in the NE intermembrane space seen by depleting NOMO in the SUN1/2 KO cell line could be a reason why LBR is accumulating in the ER, but SUN1/2 are still present in the U2OS cells that the IF experiment was done in. It is possible that NOMO somehow affects the biogenesis of LBR and SUN2 and that is why there was also an observable decrease by Western Blot of LBR levels.

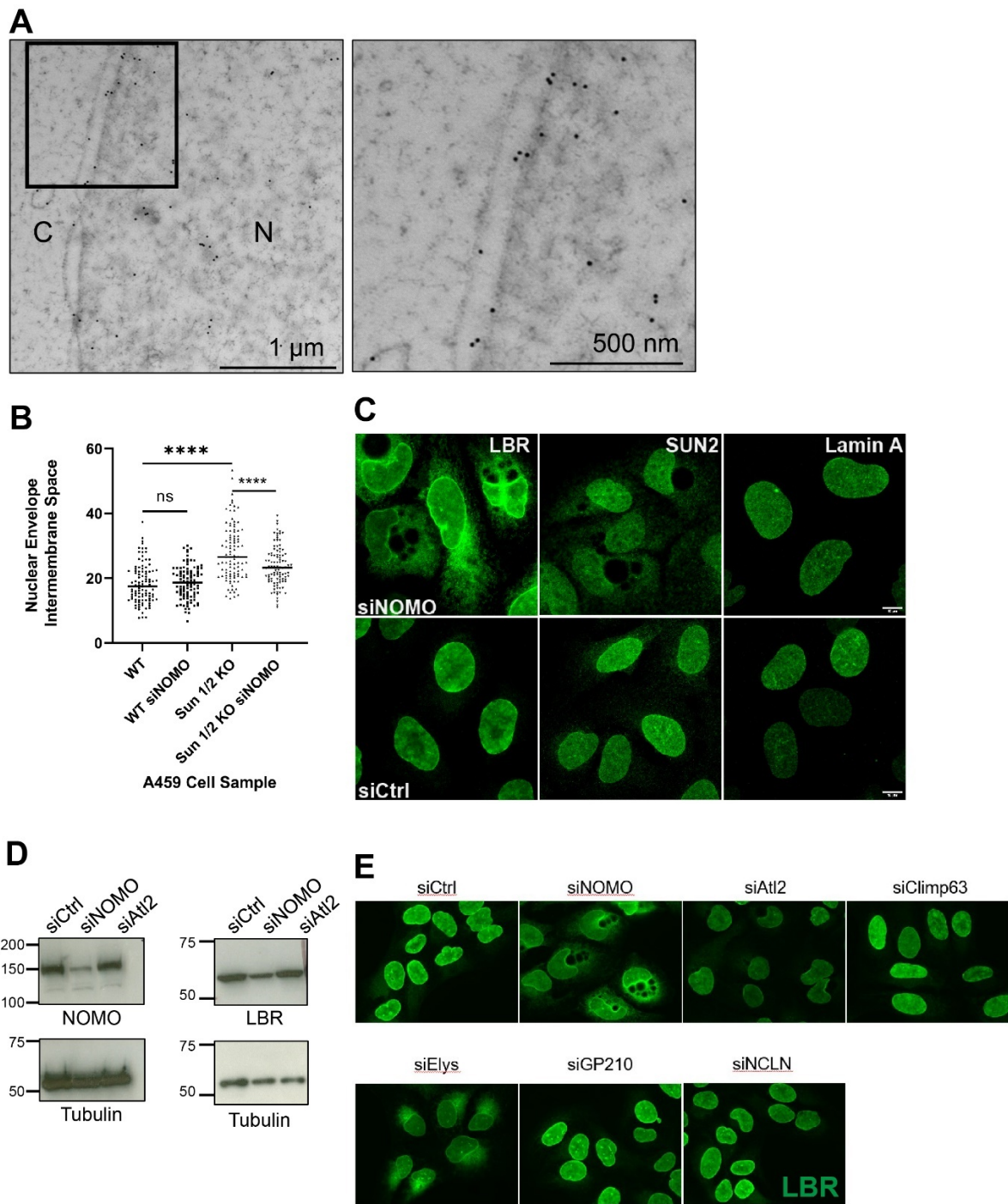


Figure 18. NOMO and the nuclear envelope.

A. EM images of immunogold labeled NOMO1-FLAG U2OS stable cell line. B. NE intermembrane space of A459 cell samples. Four asterisks = P value <0.0001. C. Representative images of U2OS cells depleted of NOMO compared to control and immunostained with the respective NE markers. D. Western Blot of siNOMO and siAtI2 U2OS cells to show the decrease of LBR occurs under siNOMO. E. Representative IF images of U2OS cells treated with the respective siRNA and probed with LBR antibody.

Chapter 4: Discussion

This thesis was dedicated to understanding the function of NOMO. We identified NOMO1 as an abundant ER constituent of unknown function (Fig. 1), motivating our functional characterization in the context of ER morphology. Notably, NOMO1 and NOMO2 have previously been observed in ER proteomes (Chen et al., 2010b; Sakai et al., 2009), but remained uncharacterized.

Our morphological characterization of NOMO depleted cells revealed a drastic rearrangement of the ER network, vacuole-like holes in the ER network were visible by IF (Fig. 3A). This phenotype was rescued by expression of not only NOMO1r, but AtI2 and Climp63 (Fig. 4). This suggests that the hole phenotype is due to an ER morphology deficit since AtI2 and Climp63 are ER shaping proteins, connecting NOMO to the network of known ER shaping proteins.

The rescue attempts with different NOMO domains proved difficult but biologically interesting due to the observable morphological effects on the ER. NOMO^{LD} caused the colocalization of the ER and lysosomes. As to date, I have not been able to find an example of a similar effect of a transfected protein in mammalian cells causing the ER to bud into circles that colocalize with enlarged lysosomes. It would be tempting to say that this colocalization of NOMO^{LD} to lysosomes and the ER shows this construct is an autophagy substrate, but if this were the case, it should have proven difficult to express and purify this protein to the levels necessary for negative stain EM. On the contrary, NOMO^{LD} purifications yielded more protein than the full-length construct. Therefore, NOMO^{LD} may be interacting with a lysosomal associated protein. NOMO-TM-CYT displayed a remarkable colocalization with microtubules. This motivated the hypothesis

that this construct could bind the microtubules, but ultimately, the TIRF assay revealed that NOMO-TM-CYT could not directly bind to microtubules. We still have not exhausted the possibility that NOMO can indirectly bind to microtubules and this should be explored in the future, for example by investigating potential interaction partners.

Ultrastructural analysis from thin-section EM of the holes that arise upon NOMO depletion revealed an enrichment of lysosome-like, electron dense structures (Fig. 8A). Consistently, autophagy was dysregulated upon NOMO or Climp63 depletion, as judged by a strong increase in LC3-II and p62 by SDS-Page/Western Blotting. NOMO depleted cells were already at saturated levels of p62 compared to the control sample treated with Baf A (Fig. 11D). Climp63 depletion caused increased p62 levels without Baf A treatment and an observable increase in LC3-II, while At12 depletion only had a minor LC3-II increase. Therefore, this autophagy dysregulation seems to be specific to NOMO and Climp63, which would show specificity to sheet proteins, even if we do not yet understand the mechanism. It is interesting that At12 depletion did demonstrate enlarged lysosomes without having the LC3-II increase. Disruption of At12 has been tangentially associated with enlarged lysosomes which was reasoned to be due to the dependence of lysosomes to track along ER tubules for transportation. There are competing theories that lysosomes determine the direction tubules grow in, so this is still an active question in the field. It will therefore be interesting to closely scrutinize the relationship between autophagy and these membrane-shaping proteins in the future.

Of note, NCLN or TMEM147 depletion did not provoke an upregulation of LC3-II (Fig. 11B), and we did not observe rearrangements of the ER network in this experimental context (Fig. 19). Thus, NOMO1 functions independently of the NCLN/TMEM147

complex. We also did not observe an induction of the UPR in NOMO depleted cells based on BiP levels, arguing against a critical function for membrane protein biogenesis. However, we cannot formally exclude subtle folding defects that would not amount to a stark UPR induction. Regardless, our observation of autophagy dysregulation upon NOMO depletion stresses the relationship of form and function of the ER. Besides imposing a distinct shape on sub-compartments of the ER, ER shaping proteins are important for defining distinct identities of these compartments.

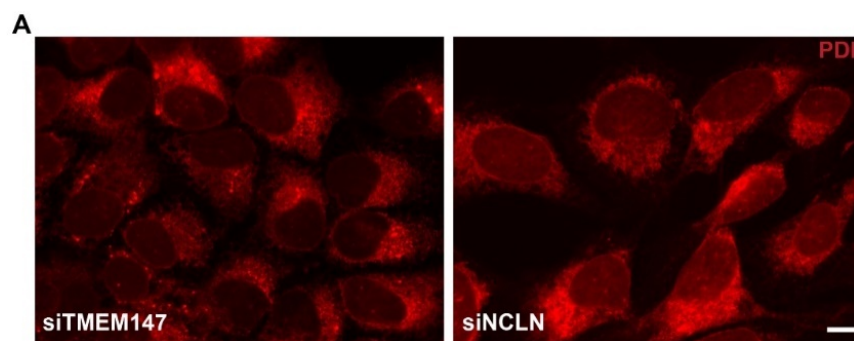


Figure 19. Depletion of NOMO interaction partners do not disrupt ER morphology.

A. U2OS cells were treated with the denoted siRNAs for 48 hrs and imaged via IF. Scale bar is 10 μ m.

Overexpression of NOMO1 resulted in a restriction of the ER intermembrane space to 33 nm (Fig. 10E). This was particularly interesting because Climp63 depletion results in a decrease of the ER lumen to 30 nm (Shen et al., 2019; Shibata et al., 2010), implying that NOMO may have a role in maintaining this smaller diameter of 30 nm. Our structural analysis revealed that NOMO1 is an extended, flexible rod of about 27 nm in length, which is close to the diameter that NOMO1 overexpression imposes on the ER lumen. We speculate that the flexibility of NOMO1 revealed by the negative stain particles may be a structural feature to prevent an overly rigid property of ER sheets. Climp63 was originally proposed to be a stable coiled coil (Vedrenne et al., 2005). More recently,

calumenin-1 was shown to regulate Climp63's distribution across ER sheets (Shen et al., 2019), allowing the ER to adapt and respond to physiological demands that require different distributions of sheets versus tubules. Therefore, there is likely a regulation mechanism for the sheet shaping mechanism of NOMO1.

The NOMO^{LD} model revealed that NOMO1 features eight discernable domains that are arranged as “beads-on-a-string” domains (Fig. 12). The POM152 structure (Upla et al., 2017) also resembles “beads on a string”. POM152 is a nuclear pore protein which also only has homology to bacterial proteins with Ig-like folds (Upla et al., 2017). Considering that Ig domains can have high structural similarity without significant sequence homology (Berardi et al., 1999), and the predicted structural similarity NOMO has to Ig-like fold proteins, our interpretation is that each of these segments correspond to one Ig-like fold domain, consistent with the secondary structure prediction showing a high beta sheet content for nearly the entire sequence of NOMO1 (Fig. S1B). Interestingly, structurally related pili proteins in bacteria can dissipate mechanical forces by acting as molecular shock absorbers (Echelmann et al., 2016). Thus, it would be interesting to test if NOMO fulfills a similar function in the ER.

While our structure-function analysis in addition to our light scattering experiments support a model of NOMO1 forming weak dimers (Fig. 10E), we were not able to unambiguously observe this oligomeric state by negative stain EM. We attribute this problem to the flexibility observed in the class averages.

How can we reconcile the dimensions of NOMO1 with our proposed role as a sheet-shaping protein? We consider three models to relate the dimensions of the NOMO1 rod to the intermembrane spacing observed upon NOMO1 overexpression. First, another,

yet unidentified protein interacts with the distal luminal end of NOMO1 at the opposite membrane (Fig. 20, I). Second, the distal luminal end of the rod-shaped molecule interacts with the membrane itself (Fig. 20, II). Third, NOMO1 dimers form antiparallel oligomers of weak affinity (Fig. 20, III) such that these interactions are not necessarily captured by SEC-MALS analysis. Indeed, a number of distinct oligomeric states of Climp63 were observed by analytical ultracentrifugation, including parallel and antiparallel dimers and trimers (Zhao and Hu, 2020). If NOMO or Climp63 require an interaction partner to induce their sheet shaping functions, then overexpressing NOMO or Climp63 would not necessarily cause a striking constriction of the ER intermembrane spacing as the quantity of the interaction partner could be a limiting component. The direct membrane interaction model (Fig. 20,II) or antiparallel oligomers model (Fig.20, III) do not rely on the presence of an interaction partner and could more readily explain the observed correlation between NOMO1 expression levels and sheet formation. Clearly, additional experiments will be required to test these models in the future.

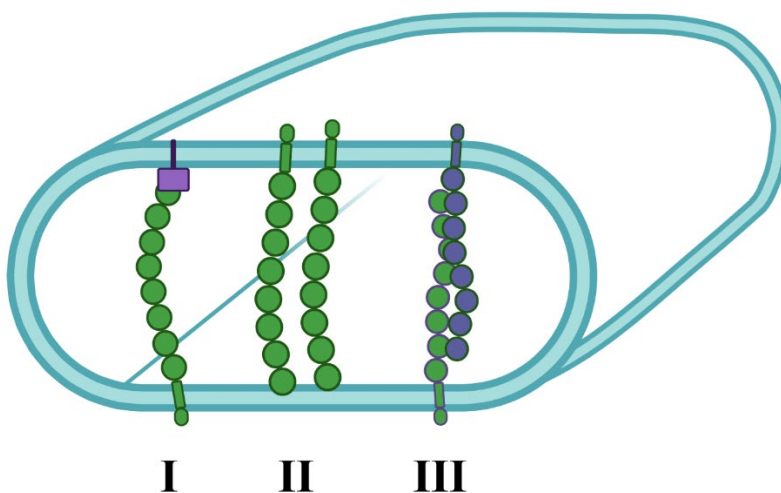


Figure 20. Models of the mechanism of NOMO regulating the ER intermembrane space.

In conclusion, we have identified a critical role for NOMO1 in sustaining the morphology of the ER. We propose a dynamic model where both the molecules responsible for membrane spacing and the interactions between them or their interaction partners are highly dynamic. This could be achieved by the inherent flexibility of membrane spacing proteins as exemplified by NOMO1, as well as low to moderate affinity interactions with binding partners at the opposite membrane. In line with this model, homotypic Climp63 interactions appear to be weak (Zhao and Hu, 2020). A dynamic model relying both on avidity of multiple weak interactions and inherent flexibility would ensure that ER spacers do not form an impediment for the secretion of bulky cargo (e.g. procollagen with 300-450 nm in length (Malhotra and Erlmann, 2015)), and allow for rapid adjustments of the ER morphology in response to physiological demand.

Chapter 5: Future Directions

There are many biophysical parameters contributing to sheet formation that we do not yet understand, leaving many open questions for future exploration. While we know Climp63 is highly expressed and, based on our mass spectrometry experiment we assume NOMO is also abundant, we do not understand how many molecules of Climp63 and/or NOMO are needed to establish and maintain a sheet. Another question is how sheet formation is regulated. Although we know that Calumenin-1 is implicated in Climp63 regulation, the mechanism of this regulation is not clear. Moreover, it remains to be explored how these molecules contribute to the mechanical stability of the ER, which can withstand forces in the range of 18 pN (Upadhyaya and Sheetz, 2004).

Interestingly, NOMO has significant structural homology to bacterial Ig-like fold proteins which have adhesion properties and can resist pulling forces on the scale of 100s of pN due to their folds and isopeptide bonds in certain beta-sheets (Echelman et al., 2016). Considering that the force to deform the ER membrane is on the scale of 10s of pN (Georgiades et al., 2017; Upadhyaya and Sheetz, 2004), conserving an intramolecular isopeptide bond would not provide an advantage to the function of NOMO in the ER but would be evolutionarily interesting as to our knowledge no mammalian protein has been shown to have an intramolecular isopeptide bond. Therefore, molecular tweezer experiments could be performed to measure how the NOMO oligomer reacts to force. While a higher resolution structure of NOMO would facilitate the design of a C-terminal and N-terminal handle, we do know that NOMO is a rod-shaped molecule and could therefore design a handle for either end of the molecule. The NOMO^{LD} construct would be easiest to start with for such designs to eliminate the need for detergent.

A cryo-EM structure of NOMO should still be an interesting problem to pursue as it would hopefully preserve the NOMO dimer. There may be different buffers that will be better at preserving the dimer through the sample preparation process. A higher resolution structure will also provide an answer to the number of Ig-folds present. Although the NOMO^{LD} model revealed 8 densities, the ends of the class averages were a bit blurry which means additional Ig folds might exist but are not yet visible due to structural flexibility.

Another question we have left unanswered is how and if NOMO truly interacts with microtubules. Our TIRF assay showed that the cytosolic domain does not directly bind to microtubules. This leaves open the possibility of indirect interaction with microtubules. Therefore, it would be worth investigating if the cytosolic domain has specific interaction partners. One way to approach this would be to perform an immunoprecipitation of the cytosolic domain and submit the elution for mass spectrometry analysis. One concern is that the transmembrane domain was important for the striking IF phenotype of the construct colocalizing to the MT. Therefore, an additional immunoprecipitation could be performed with the TM-CYT construct. It would also be interesting to determine the interaction partners of the NOMO^{LD} construct, especially if there were an interaction partner different from NOMO1-FLAG. A difference in interaction partners may help understand the enrichment of NOMO^{LD}-FLAG in the lysosomes, potentially illuminating the connection to lysosome biology.

At this point, we observed that autophagy is affected by both NOMO and Climp63 depletion, however if this is an indirect effect of disrupting sheet morphology or due to a

more specific function of these sheet shaping proteins in this context remains to be determined.

Another potential ER function that NOMO could be involved in is the biogenesis of multi-transmembrane proteins. NCLN and TMEM147 are crucial to forming the Sec61 complex for a certain subset of transmembrane proteins (McGilvray et al., 2020). One way to address if NOMO could play a role in this complex would be to deplete NOMO and measure the protein levels of the TM proteins that require the Sec61/NCLN/TMEM147 complex for proper folding. If the proteins have decreased levels under NOMO depletion, that would show NOMO is functionally tied to the biogenesis of these proteins. Alternatively, the NOMO Ig-like folds may play a role in weakly binding the TM proteins undergoing folding to help stabilize them in the membrane, or NOMO might help stabilize the local membrane area for the Sec61/NCLN/TMEM147 complex. One biophysical method to test if NOMO could be stabilizing a particular membrane area would be to use a fluorescence recovery after photobleaching (FRAP) based assay. FRAP assays have been used to show that tubule shaping proteins form immobile oligomers to stabilize tubule architecture (Shibata et al., 2008).

The best *in vitro* method to unambiguously prove that NOMO and Climp63 are sheet spacers would be to incorporate these purified proteins into liposomes in conjunction with EM imaging. Tubule shaping proteins were established as clearly having tubule shaping properties because of these *in vitro* liposome assays. Lunapark was also successfully incorporated into liposomes and shown to be responsible for disc stacking (Wang et al., 2018). The only example of Climp63 incorporated into liposomes showed the Climp63 luminal domain on the outside of the liposome (Shen et al., 2019). This

creates an interesting question about the establishment versus the maintenance of sheets. The default form of a liposome is a sphere because this is the lowest energy state. When tubule shaping proteins were added to these liposomes, they only had to incorporate into the outer lipid layer of the membrane where they could then oligomerize to elongate the liposome and form a tubule. Incorporating a sheet protein into a liposome would require sufficient protein to force that liposome into a flatter sheet structure. Specific tubule shaping proteins to stabilize the high curvature edges that would be formed if sheet proteins were establishing a flat membrane area would likely be required as well. Another method would be to incorporate NOMO into nanodiscs. Incorporating NOMO into nanodiscs might reveal the oligomeric state of NOMO and we would be able to observe if NOMO forms antiparallel dimers if we observed two nanodiscs connected by NOMO molecules.

While ER morphology has been modeled (Shemesh et al., 2014) to depend on concentrations of tubule shaping proteins and lunapark, the difficulty in establishing a sheet *in vitro* leaves a gap in our understanding of ER morphology.

Lastly, a major open question pertains to dynamics of the ER as the ER is a highly dynamic organelle. The ER constantly rearranges to perform the necessary functions of interacting with other organelles, grows and moves with the cell, and generate tubules or sheets in response to cell needs. However, the cell biological data I have presented relies on fixed cells. One example of how live cell imaging data can drastically change our understanding of ER dynamics is from the effects of Atlastin GTPase mutants on tubule morphology. Atlastin depletion and mutants have largely been shown to cause long unbranched tubules as evident from immunofluorescence imaging. When live cell imaging

was employed to image cells expressing an Atlastin GTPase mutant, it revealed that this construct causes the ER tubules to become small vesicles, which were not captured by IF (Wang et al., 2016). Therefore, capturing the dynamics of the ER could further inform our understanding of how NOMO depletion affects ER morphology. Does NOMO depletion affect tubule dynamics at all and is that why we observe holes under both NOMO depletion and At12 depletion? Another question live cell imaging could address is how these holes arise. We believe these holes to be generally flat spheres in shape, but now that we know that the holes are enriched in lysosomes, the question arises as to whether the holes arise from lack of structural support that give way to lysosomes accumulating in the holes. Alternatively, lysosomes may become enlarged, directly or indirectly because of NOMO depletion, and slowly exclude the ER out of this area.

In conclusion, while we have learned much about the molecular function of NOMO, there is much more to be discovered about the mechanistic details of how NOMO contributes to the ER intermembrane space and the functional relationship between membrane spacing proteins and organelle functions.

References

- Abrisch, R.G., S.C. Gumbin, B.T. Wisniewski, L.L. Lackner, and G.K. Voeltz. 2020. Fission and fusion machineries converge at ER contact sites to regulate mitochondrial morphology. *J Cell Biol.* 219.
- Albright, R.A., J.L. Ibar, C.U. Kim, S.M. Gruner, and J.H. Morais-Cabral. 2006. The RCK domain of the KtrAB K⁺ transporter: multiple conformations of an octameric ring. *Cell.* 126:1147-1159.
- Berardi, M.J., C. Sun, M. Zehr, F. Abildgaard, J. Peng, N.A. Speck, and J.H. Bushweller. 1999. The Ig fold of the core binding factor alpha Runt domain is a member of a family of structurally and functionally related Ig-fold DNA-binding domains. *Structure.* 7:1247-1256.
- Bian, X., R.W. Klemm, T.Y. Liu, M. Zhang, S. Sun, X. Sui, X. Liu, T.A. Rapoport, and J. Hu. 2011. Structures of the atlastin GTPase provide insight into homotypic fusion of endoplasmic reticulum membranes. *Proc Natl Acad Sci U S A.* 108:3976-3981.
- Blackstone, C., C.J. O'Kane, and E. Reid. 2011. Hereditary spastic paraplegias: membrane traffic and the motor pathway. *Nat Rev Neurosci.* 12:31-42.
- Buchan, D.W.A., and D.T. Jones. 2019. The PSIPRED Protein Analysis Workbench: 20 years on. *Nucleic Acids Res.* 47:W402-W407.
- Byrnes, L.J., and H. Sonderrmann. 2011. Structural basis for the nucleotide-dependent dimerization of the large G protein atlastin-1/SPG3A. *Proc Natl Acad Sci U S A.* 108:2216-2221.
- Cain, N.E., E.C. Tapley, K.L. McDonald, B.M. Cain, and D.A. Starr. 2014. The SUN protein UNC-84 is required only in force-bearing cells to maintain nuclear envelope architecture. *J Cell Biol.* 206:163-172.
- Chen, Q., Y. Xiao, P. Chai, P. Zheng, J. Teng, and J. Chen. 2019. ATL3 Is a Tubular ER-Phagy Receptor for GABARAP-Mediated Selective Autophagy. *Curr Biol.* 29:846-855 e846.
- Chen, S., P. Novick, and S. Ferro-Novick. 2012. ER network formation requires a balance of the dynamin-like GTPase Sey1p and the Lunapark family member Lnp1p. *Nat Cell Biol.* 14:707-716.

- Chen, X., A. Karnovsky, M.D. Sans, P.C. Andrews, and J.A. Williams. 2010a. Molecular characterization of the endoplasmic reticulum: insights from proteomic studies. *Proteomics*. 10:4040-4052.
- Chen, X., M.D. Sans, J.R. Strahler, A. Karnovsky, S.A. Ernst, G. Michailidis, P.C. Andrews, and J.A. Williams. 2010b. Quantitative organellar proteomics analysis of rough endoplasmic reticulum from normal and acute pancreatitis rat pancreas. *J Proteome Res*. 9:885-896.
- Chitwood, P.J., and R.S. Hegde. 2020. An intramembrane chaperone complex facilitates membrane protein biogenesis. *Nature*. 584:630-634.
- Chiurchiu, V., M. Maccarrone, and A. Orlacchio. 2014. The role of reticulons in neurodegenerative diseases. *Neuromolecular Med*. 16:3-15.
- Choudhuri, K., D. Wiseman, M.H. Brown, K. Gould, and P.A. van der Merwe. 2005. T-cell receptor triggering is critically dependent on the dimensions of its peptide-MHC ligand. *Nature*. 436:578-582.
- Coutts, A.S., and N.B. La Thangue. 2015. Actin nucleation by WH2 domains at the autophagosome. *Nat Commun*. 6:7888.
- de Araujo, M.E.G., G. Liebscher, M.W. Hess, and L.A. Huber. 2020. Lysosomal size matters. *Traffic*. 21:60-75.
- Dettmer, U., P.H. Kuhn, C. Abou-Ajram, S.F. Lichtenthaler, M. Kruger, E. Kremmer, C. Haass, and C. Haffner. 2010. Transmembrane protein 147 (TMEM147) is a novel component of the Nicalin-NOMO protein complex. *J Biol Chem*. 285:26174-26181.
- Duan, L., R.E. Perez, B. Davaadelger, E.N. Dedkova, L.A. Blatter, and C.G. Maki. 2015. p53-regulated autophagy is controlled by glycolysis and determines cell fate. *Oncotarget*. 6:23135-23156.
- Echelmann, D.J., J. Alegre-Cebollada, C.L. Badilla, C. Chang, H. Ton-That, and J.M. Fernandez. 2016. CnaA domains in bacterial pili are efficient dissipaters of large mechanical shocks. *Proc Natl Acad Sci U S A*. 113:2490-2495.
- Espadas, J., D. Pendin, R. Bocanegra, A. Escalada, G. Misticoni, T. Trevisan, A. Velasco Del Olmo, A. Montagna, S. Bova, B. Ibarra, P.I. Kuzmin, P.V. Bashkirov,

- A.V. Shnyrova, V.A. Frolov, and A. Daga. 2019. Dynamic constriction and fission of endoplasmic reticulum membranes by reticulon. *Nat Commun.* 10:5327.
- Friedman, J.R., L.L. Lackner, M. West, J.R. DiBenedetto, J. Nunnari, and G.K. Voeltz. 2011. ER tubules mark sites of mitochondrial division. *Science.* 334:358-362.
- Friedman, J.R., B.M. Webster, D.N. Mastronarde, K.J. Verhey, and G.K. Voeltz. 2010. ER sliding dynamics and ER-mitochondrial contacts occur on acetylated microtubules. *J Cell Biol.* 190:363-375.
- Gao, W.L., M. Liu, Y. Yang, H. Yang, Q. Liao, Y. Bai, Y.X. Li, D. Li, C. Peng, and Y.L. Wang. 2012. The imprinted H19 gene regulates human placental trophoblast cell proliferation via encoding miR-675 that targets Nodal Modulator 1 (NOMO1). *RNA Biol.* 9:1002-1010.
- Georgiades, P., V.J. Allan, G.D. Wright, P.G. Woodman, P. Udommai, M.A. Chung, and T.A. Waigh. 2017. The flexibility and dynamics of the tubules in the endoplasmic reticulum. *Sci Rep.* 7:16474.
- Grumati, P., G. Morozzi, S. Holper, M. Mari, M.I. Harwardt, R. Yan, S. Muller, F. Reggiori, M. Heilemann, and I. Dikic. 2017. Full length RTN3 regulates turnover of tubular endoplasmic reticulum via selective autophagy. *Elife.* 6.
- Haffner, C., U. Dettmer, T. Weiler, and C. Haass. 2007. The Nicastrin-like protein Nicalin regulates assembly and stability of the Nicalin-nodal modulator (NOMO) membrane protein complex. *J Biol Chem.* 282:10632-10638.
- Haffner, C., M. Frauli, S. Topp, M. Irmeler, K. Hofmann, J.T. Regula, L. Bally-Cuif, and C. Haass. 2004. Nicalin and its binding partner Nomo are novel Nodal signaling antagonists. *EMBO J.* 23:3041-3050.
- Helenius, A., and M. Aebi. 2004. Roles of N-linked glycans in the endoplasmic reticulum. *Annu Rev Biochem.* 73:1019-1049.
- Hoyer, M.J., P.J. Chitwood, C.C. Ebmeier, J.F. Striepen, R.Z. Qi, W.M. Old, and G.K. Voeltz. 2018. A Novel Class of ER Membrane Proteins Regulates ER-Associated Endosome Fission. *Cell.* 175:254-265 e214.
- Hu, J., Y. Shibata, C. Voss, T. Shemesh, Z. Li, M. Coughlin, M.M. Kozlov, T.A. Rapoport, and W.A. Prinz. 2008. Membrane proteins of the endoplasmic reticulum induce high-curvature tubules. *Science.* 319:1247-1250.

- Hu, J., Y. Shibata, P.P. Zhu, C. Voss, N. Rismanchi, W.A. Prinz, T.A. Rapoport, and C. Blackstone. 2009. A class of dynamin-like GTPases involved in the generation of the tubular ER network. *Cell*. 138:549-561.
- Hung, V., N.D. Udeshi, S.S. Lam, K.H. Loh, K.J. Cox, K. Pedram, S.A. Carr, and A.Y. Ting. 2016. Spatially resolved proteomic mapping in living cells with the engineered peroxidase APEX2. *Nat Protoc*. 11:456-475.
- Hung, V., P. Zou, H.W. Rhee, N.D. Udeshi, V. Cracan, T. Svinkina, S.A. Carr, V.K. Mootha, and A.Y. Ting. 2014. Proteomic mapping of the human mitochondrial intermembrane space in live cells via ratiometric APEX tagging. *Mol Cell*. 55:332-341.
- Jozsef, L., K. Tashiro, A. Kuo, E.J. Park, A. Skoura, S. Albinsson, F. Rivera-Molina, K.D. Harrison, Y. Iwakiri, D. Toomre, and W.C. Sessa. 2014. Reticulon 4 is necessary for endoplasmic reticulum tubulation, STIM1-Orai1 coupling, and store-operated calcium entry. *J Biol Chem*. 289:9380-9395.
- Kelley, L.A., S. Mezulis, C.M. Yates, M.N. Wass, and M.J. Sternberg. 2015. The Pyre2 web portal for protein modeling, prediction and analysis. *Nat Protoc*. 10:845-858.
- Klemm, R.W., J.P. Norton, R.A. Cole, C.S. Li, S.H. Park, M.M. Crane, L. Li, D. Jin, A. Boye-Doe, T.Y. Liu, Y. Shibata, H. Lu, T.A. Rapoport, R.V. Farese, Jr., C. Blackstone, Y. Guo, and H.Y. Mak. 2013. A conserved role for atlastin GTPases in regulating lipid droplet size. *Cell Rep*. 3:1465-1475.
- Klopfenstein, D.R., F. Kappeler, and H.P. Hauri. 1998. A novel direct interaction of endoplasmic reticulum with microtubules. *EMBO J*. 17:6168-6177.
- Lam, S.S., J.D. Martell, K.J. Kamer, T.J. Deerinck, M.H. Ellisman, V.K. Mootha, and A.Y. Ting. 2015. Directed evolution of APEX2 for electron microscopy and proximity labeling. *Nat Methods*. 12:51-54.
- Lee, S., and S. Bahmanyar. 2020. The Endoplasmic Reticulum Regulates Membraneless Organelles through Contact Sites. *Biochemistry*. 59:1716-1717.
- Lee, S.H., S. Hadipour-Lakmehsari, H.R. Murthy, N. Gibb, T. Miyake, A.C.T. Teng, J. Cosme, J.C. Yu, M. Moon, S. Lim, V. Wong, P. Liu, F. Billia, R. Fernandez-Gonzalez, I. Stagljar, P. Sharma, T. Kislinger, I.C. Scott, and A.O. Gramolini.

2020. REEP5 depletion causes sarco-endoplasmic reticulum vacuolization and cardiac functional defects. *Nat Commun.* 11:965.
- Lee, S.Y., M.G. Kang, J.S. Park, G. Lee, A.Y. Ting, and H.W. Rhee. 2016. APEX Fingerprinting Reveals the Subcellular Localization of Proteins of Interest. *Cell Rep.* 15:1837-1847.
- Liang, J.R., E. Lingeman, S. Ahmed, and J.E. Corn. 2018. Atlastins remodel the endoplasmic reticulum for selective autophagy. *J Cell Biol.* 217:3354-3367.
- Ma, Y., and L.M. Hendershot. 2001. The unfolding tale of the unfolded protein response. *Cell.* 107:827-830.
- Malhotra, V., and P. Erlmann. 2015. The pathway of collagen secretion. *Annu Rev Cell Dev Biol.* 31:109-124.
- Matlack, K.E., W. Mothes, and T.A. Rapoport. 1998. Protein translocation: tunnel vision. *Cell.* 92:381-390.
- McGilvray, P.T., S.A. Anghel, A. Sundaram, F. Zhong, M.J. Trnka, J.R. Fuller, H. Hu, A.L. Burlingame, and R.J. Keenan. 2020. An ER translocon for multi-pass membrane protein biogenesis. *Elife.* 9.
- Meldolesi, J., and T. Pozzan. 1998. The endoplasmic reticulum Ca²⁺ store: a view from the lumen. *Trends Biochem Sci.* 23:10-14.
- Miller, O.K., M.J. Banfield, and U. Schwarz-Linek. 2018. A new structural class of bacterial thioester domains reveals a slipknot topology. *Protein Sci.* 27:1651-1660.
- Morin-Leisk, J., S.G. Saini, X. Meng, A.M. Makhov, P. Zhang, and T.H. Lee. 2011. An intramolecular salt bridge drives the soluble domain of GTP-bound atlastin into the postfusion conformation. *J Cell Biol.* 195:605-615.
- Moss, T.J., C. Andreatza, A. Verma, A. Daga, and J.A. McNew. 2011. Membrane fusion by the GTPase atlastin requires a conserved C-terminal cytoplasmic tail and dimerization through the middle domain. *Proc Natl Acad Sci U S A.* 108:11133-11138.
- Oertle, T., M. Klinger, C.A. Stuermer, and M.E. Schwab. 2003. A reticular rhapsody: phylogenetic evolution and nomenclature of the RTN/Nogo gene family. *FASEB J.* 17:1238-1247.

- Orso, G., D. Pendin, S. Liu, J. Toretto, T.J. Moss, J.E. Faust, M. Micaroni, A. Egorova, A. Martinuzzi, J.A. McNew, and A. Daga. 2009. Homotypic fusion of ER membranes requires the dynamin-like GTPase atlastin. *Nature*. 460:978-983.
- Palade, G.E. 1956. The endoplasmic reticulum. *J Biophys Biochem Cytol*. 2:85-98.
- Park, S.H., P.P. Zhu, R.L. Parker, and C. Blackstone. 2010. Hereditary spastic paraplegia proteins REEP1, spastin, and atlastin-1 coordinate microtubule interactions with the tubular ER network. *J Clin Invest*. 120:1097-1110.
- Pawar, S., R. Ungricht, P. Tiefenboeck, J.C. Leroux, and U. Kutay. 2017. Efficient protein targeting to the inner nuclear membrane requires Atlastin-dependent maintenance of ER topology. *Elife*. 6.
- Perea, J., J.L. Garcia, J. Perez, D. Rueda, M. Arriba, Y. Rodriguez, M. Urioste, and R. Gonzalez-Sarmiento. 2017. NOMO-1 gene is deleted in early-onset colorectal cancer. *Oncotarget*. 8:24429-24436.
- Powers, R.E., S. Wang, T.Y. Liu, and T.A. Rapoport. 2017. Reconstitution of the tubular endoplasmic reticulum network with purified components. *Nature*. 543:257-260.
- Rhee, H.W., P. Zou, N.D. Udeshi, J.D. Martell, V.K. Mootha, S.A. Carr, and A.Y. Ting. 2013. Proteomic mapping of mitochondria in living cells via spatially restricted enzymatic tagging. *Science*. 339:1328-1331.
- Rowland, A.A., P.J. Chitwood, M.J. Phillips, and G.K. Voeltz. 2014. ER contact sites define the position and timing of endosome fission. *Cell*. 159:1027-1041.
- Sakai, K., R. Hamanaka, H. Yuki, and M. Watanabe. 2009. A novel fractionation method of the rough ER integral membrane proteins; resident proteins versus exported proteins? *Proteomics*. 9:3036-3046.
- Scheres, S.H. 2012. RELION: implementation of a Bayesian approach to cryo-EM structure determination. *J Struct Biol*. 180:519-530.
- Schroeder, L.K., A.E.S. Barentine, H. Merta, S. Schweighofer, Y. Zhang, D. Baddeley, J. Bewersdorf, and S. Bahmanyar. 2019. Dynamic nanoscale morphology of the ER surveyed by STED microscopy. *J Cell Biol*. 218:83-96.
- Schweitzer, Y., T. Shemesh, and M.M. Kozlov. 2015. A Model for Shaping Membrane Sheets by Protein Scaffolds. *Biophys J*. 109:564-573.

- Shemesh, T., R.W. Klemm, F.B. Romano, S. Wang, J. Vaughan, X. Zhuang, H. Tukachinsky, M.M. Kozlov, and T.A. Rapoport. 2014. A model for the generation and interconversion of ER morphologies. *Proc Natl Acad Sci U S A*. 111:E5243-5251.
- Shen, B., P. Zheng, N. Qian, Q. Chen, X. Zhou, J. Hu, J. Chen, and J. Teng. 2019. Calumenin-1 Interacts with Climp63 to Cooperatively Determine the Luminal Width and Distribution of Endoplasmic Reticulum Sheets. *iScience*. 22:70-80.
- Shen, M.M. 2007. Nodal signaling: developmental roles and regulation. *Development*. 134:1023-1034.
- Shibata, Y., T. Shemesh, W.A. Prinz, A.F. Palazzo, M.M. Kozlov, and T.A. Rapoport. 2010. Mechanisms determining the morphology of the peripheral ER. *Cell*. 143:774-788.
- Shibata, Y., C. Voss, J.M. Rist, J. Hu, T.A. Rapoport, W.A. Prinz, and G.K. Voeltz. 2008. The reticulon and DP1/Yop1p proteins form immobile oligomers in the tubular endoplasmic reticulum. *J Biol Chem*. 283:18892-18904.
- Slotboom, D.J., R.H. Duurkens, K. Olieman, and G.B. Erkens. 2008. Static light scattering to characterize membrane proteins in detergent solution. *Methods*. 46:73-82.
- Tang, G., L. Peng, P.R. Baldwin, D.S. Mann, W. Jiang, I. Rees, and S.J. Ludtke. 2007. EMAN2: an extensible image processing suite for electron microscopy. *J Struct Biol*. 157:38-46.
- Tanida, I., T. Ueno, and E. Kominami. 2008. LC3 and Autophagy. *Methods Mol Biol*. 445:77-88.
- Testerink, N., M.H. van der Sanden, M. Houweling, J.B. Helms, and A.B. Vaandrager. 2009. Depletion of phosphatidylcholine affects endoplasmic reticulum morphology and protein traffic at the Golgi complex. *J Lipid Res*. 50:2182-2192.
- Upadhyaya, A., and M.P. Sheetz. 2004. Tension in tubulovesicular networks of Golgi and endoplasmic reticulum membranes. *Biophys J*. 86:2923-2928.
- Upla, P., S.J. Kim, P. Sampathkumar, K. Dutta, S.M. Cahill, I.E. Chemmama, R. Williams, J.B. Bonanno, W.J. Rice, D.L. Stokes, D. Cowburn, S.C. Almo, A. Sali, M.P. Rout, and J. Fernandez-Martinez. 2017. Molecular Architecture of the Major

- Membrane Ring Component of the Nuclear Pore Complex. *Structure*. 25:434-445.
- Vajente, N., R. Norante, N. Redolfi, A. Daga, P. Pizzo, and D. Pendin. 2019. Microtubules Stabilization by Mutant Spastin Affects ER Morphology and Ca(2+) Handling. *Front Physiol*. 10:1544.
- Vedrenne, C., D.R. Klopfenstein, and H.P. Hauri. 2005. Phosphorylation controls CLIMP-63-mediated anchoring of the endoplasmic reticulum to microtubules. *Mol Biol Cell*. 16:1928-1937.
- Veesler, D., S. Blangy, M. Siponen, R. Vincentelli, C. Cambillau, and G. Sciara. 2009. Production and biophysical characterization of the CorA transporter from *Methanosarcina mazei*. *Anal Biochem*. 388:115-121.
- Voeltz, G.K., W.A. Prinz, Y. Shibata, J.M. Rist, and T.A. Rapoport. 2006. A class of membrane proteins shaping the tubular endoplasmic reticulum. *Cell*. 124:573-586.
- Walter, P., and D. Ron. 2011. The unfolded protein response: from stress pathway to homeostatic regulation. *Science*. 334:1081-1086.
- Wang, N., L.D. Clark, Y. Gao, M.M. Kozlov, T. Shemesh, and T.A. Rapoport. 2021. Mechanism of membrane-curvature generation by ER-tubule shaping proteins. *Nat Commun*. 12:568.
- Wang, S., R.E. Powers, V.A. Gold, and T.A. Rapoport. 2018. The ER morphology-regulating lunapark protein induces the formation of stacked bilayer discs. *Life Sci Alliance*. 1:e201700014.
- Wang, S., H. Tukachinsky, F.B. Romano, and T.A. Rapoport. 2016. Cooperation of the ER-shaping proteins atlastin, lunapark, and reticulons to generate a tubular membrane network. *Elife*. 5.
- Yates, A.D., P. Achuthan, W. Akanni, J. Allen, J. Allen, J. Alvarez-Jarreta, M.R. Amode, I.M. Armean, A.G. Azov, R. Bennett, J. Bhai, K. Billis, S. Boddu, J.C. Marugán, C. Cummins, C. Davidson, K. Dodiya, R. Fatima, A. Gall, C.G. Giron, L. Gil, T. Grego, L. Haggerty, E. Haskell, T. Hourlier, O.G. Izuogu, S.H. Janacek, T. Juettemann, M. Kay, I. Lavidas, T. Le, D. Lemos, J.G. Martinez, T. Maurel, M. McDowall, A. McMahan, S. Mohanan, B. Moore, M. Nuhn, D.N. Oheh, A. Parker,

- A. Parton, M. Patricio, M.P. Sakthivel, A.I. Abdul Salam, B.M. Schmitt, H. Schuilenburg, D. Sheppard, M. Sycheva, M. Szuba, K. Taylor, A. Thormann, G. Threadgold, A. Vullo, B. Walts, A. Winterbottom, A. Zadissa, M. Chakiachvili, B. Flint, A. Frankish, S.E. Hunt, G. Ilesley, M. Kostadima, N. Langridge, J.E. Loveland, F.J. Martin, J. Morales, J.M. Mudge, M. Muffato, E. Perry, M. Ruffier, S.J. Trevanion, F. Cunningham, K.L. Howe, D.R. Zerbino, and P. Flicek. 2019. Ensembl 2020. *Nucleic Acids Research*. 48:D682-D688.
- Yoshii, S.R., and N. Mizushima. 2017. Monitoring and Measuring Autophagy. *Int J Mol Sci*. 18.
- Zhang, H., C. Xu, R. Yang, H. Chen, X. Kong, L. Qian, Y. Sheng, and W. Sun. 2015. Silencing of nodal modulator 1 inhibits the differentiation of P19 cells into cardiomyocytes. *Exp Cell Res*. 331:369-376.
- Zhao, G., P.P. Zhu, B. Renvoise, L. Maldonado-Baez, S.H. Park, and C. Blackstone. 2016. Mammalian knock out cells reveal prominent roles for atlastin GTPases in ER network morphology. *Exp Cell Res*. 349:32-44.
- Zhao, J., and J. Hu. 2020. Self-Association of Purified Reconstituted ER Luminal Spacer Climp63. *Frontiers in Cell and Developmental Biology*. 8.
- Zhou, X., Y. He, X. Huang, Y. Guo, D. Li, and J. Hu. 2019. Reciprocal regulation between lunapark and atlastin facilitates ER three-way junction formation. *Protein Cell*. 10:510-525.
- Zhu, P.P., A. Patterson, B. Lavoie, J. Stadler, M. Shoeb, R. Patel, and C. Blackstone. 2003. Cellular localization, oligomerization, and membrane association of the hereditary spastic paraplegia 3A (SPG3A) protein atlastin. *J Biol Chem*. 278:49063-49071.